

Master's thesis

Three-dimensional strain rate in the heart muscle: new insight into cardiac function

Lasse Totland

Biological and Medical Physics
60 ECTS study points

Institute of Experimental Medical Research
Oslo University Hospital

Spring 2024



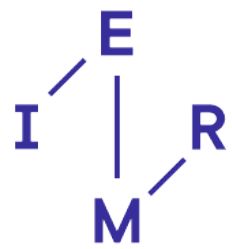
Lasse Totland

Three-dimensional strain rate in
the heart muscle: new insight
into cardiac function

Supervisor:
Emil Knut Stenersen Espe

Scientific environment

This thesis was carried out at the Institute of Experimental Medical Research, Oslo University Hospital (IEMR, OUS) as part of the MSc study program "Biological and Medical Physics" at the Department of Physics, University of Oslo.



Acknowledgements

Thank someone

(thank medfys for letting me hold a talk at their conference?) (thank iemr, emil) (thank my boys)

Your Name
Place, Date

Abstract

Background: Heart failure (HF) is a crippling and progressive disease, and the main cause of hospitalization among patients over 65 in Europe. Left ventricular (LV) strain measurements can be used as an early indicator of myocardial dysfunction after infarct. Previous studies have proven the viability of deriving strain rate tensors from motion-encoded MRI (tissue phase mapping, TPM) to describe the direction and magnitude of strain rate on voxel scale, though this method has not yet been implemented to investigate heart dysfunction.

Aim: Our aim was to apply this method to gain new insight on regional myocardial function in rat hearts after myocardial infarction using 3D TPM data of the left ventricle with high spatial/temporal resolution.

Materials & Methods: First, to validate the method, a framework developed in Python was used to reproduce global strain and strain rate curves from 2D short-axis cross-sections of the left ventricle that were compared to literature for established methods. The framework was then used to assess the 3D direction of strain rate independently from the conventions of radial, circumferential and longitudinal axes as well as the development of these measurements as a function of days after infarction. The measurements were compared to a sham-operated control group.

Results: Global values calculated using our framework agreed well to the literature. Regional analysis revealed that the strain rate magnitude is reduced in the infarcted area and that this area has reduced strain compared to the other wall sections and the sham control curves. Our data also indicate that the strain rate angles, relative to radial direction from heart center, become less homogenous over time after infarct.

Conclusion: We have shown, for the first time, that strain rate tensor analysis of TPM MRI data is a viable tool to assess regional myocardial strain and strain rate in rat hearts. Our framework also allows for measurement of strain rate directions independently of conventional heart geometry, though the implications of our observations here need further investigation.

Contents

Scientific environment	i
Acknowledgements	iii
Abstract	v
Abbreviations	1
1 Introduction	3
2 Theory	5
2.1 MR theory overview	5
2.1.1 The spin	5
2.1.2 RF pulse	6
2.1.3 Fourier transform	7
2.1.4 K-space	7
2.1.5 Pulse sequences	7
2.1.6 Motion encoded MRI / PC-MRI	7
2.1.7 MRI geometry	7
2.2 Heart physiology	8
2.2.1 Heart anatomy and the cardiac cycle	8
2.2.2 Myocardial infarction	10
2.3 Strain and strain rate analysis	11
3 Material and Methods	15
3.1 Data overview	15
3.1.1 Rat MI model	15
3.1.2 MRI Acquisition	15
3.2 LV segmentation models	16
3.3 Strain rate tensor analysis framework	17
3.3.1 The velocity field	17
3.3.2 Numeric implementation of Selskog method	19
3.3.3 Ellipsoid tensor visualization	20
3.3.4 Eigenvector decomposition	22
3.3.5 Global LV strain rate	23
3.3.6 Global LV strain	24

3.3.7	Regional strain and strain rate	26
3.3.8	Eigenvector angle distributions	27
3.3.9	Framework adjustments for 3D analysis	27
3.4	Statistical analysis	28
3.4.1	Parameter overview	29
3.4.2	Linear regression	30
3.4.3	T-tests	31
4	Results	33
4.1	2D strain rate tensor analysis	33
4.1.1	Visualization	33
4.1.2	Global strain rate and strain	34
4.1.3	Regional strain rate and strain	35
4.1.4	Eigenvector angle distribution	35
4.1.5	MI progression	37
4.2	3D strain rate tensor analysis	41
4.2.1	Global strain rate and strain	41
4.2.2	Regional strain rate and strain	41
4.2.3	Eigenvector angle distribution	41
4.2.4	(Progression / statistical analysis)	41
5	Discussion	43
5.1	2D strain rate tensor analysis	43
5.1.1	Tensor Visualization	43
5.1.2	Global strain rate and strain	44
5.1.3	Regional strain rate and strain	45
5.1.4	Eigenvector angle distribution	46
5.2	3D strain rate tensor analysis	47
5.3	Limitations and future research (move to conclusion?)	47
6	Conclusion	49
	Bibliography	54
	Appendix	55

Abbreviations

MRI	Magnetic Resonance Imaging
HF	Heart Failure
SV	Stroke Volume
EDV	End-Diastolic Volume
LV	Left Ventricle
TPM	Tissue Phase Mapping
EF	Ejection Fraction
STE	Speckle Tracking Echocardiography
CMR	Cardiovascular Magnetic Resonance
CMR-FT	CMR Feature Tracking
PC-MRI	Phase Contrast MRI
MI	Myocardial Infarction
SHAX	Short Axis
RF	Radio Frequency
FT	Fourier Transform
LA	Left Atrium
RA	Right Atrium
RV	Right Ventricle
LGE	Late Gadolinium Enhancement
SE	Standard Error

Abbreviations of all parameter names used in the statistical analysis can be found in section 3.4.1.

Chapter 1

Introduction

Heart Failure (HF) is a life-threatening disease that affects more than 64 million people worldwide, and attempts to decrease its social and economic burden have become a major priority in global public health (1). Morbidity remains high, the diagnosis is increasing in prevalence with an aging population and the healthcare expenditure is projected to increase dramatically (2). HF significantly affects quality of life by impairing social and mental health (3). Despite being a widely researched topic, many aspects of the disease remains unknown.

HF is characterized by a reduction in the heart's ability to pump a sufficient amount of blood to the body (4). This can be due to decreased blood supply to certain parts of the heart muscle tissue (myocardium) leading to areas of necrotic infarct tissue that can't contribute to mechanical pumping work. This can lead to a heart attack, which is also referred to as "myocardial infarction" (MI) (5). A parameter that can measure reduced myocardial function is the ejection fraction (EF), which describes the ability of the left ventricle (LV) to deform relative to its maximum volume: the end-diastolic volume (EDV). EF is defined as the ratio between the stroke volume (SV) and the EDV, where the SV is the difference between the EDV and the smallest LV volume during the cardiac cycle (6).

While a decrease in EF can be an accurate indicator of global reduction in myocardial function by revealing reduced deformability, this parameter is not sensitive to regional changes and tends to be unable to show significant reduction in EF measurements before the late stages of HF (7). An alternative parameter is "strain", which is a measure of deformation of an object relative to its initial length (8). It has been shown that regional strain analysis of the LV can be an early indicator of myocardial dysfunction by quantifying the amount of deformation in different areas of the LV myocardium (9). This kind of analysis studies strain or strain rate along radial, circumferential and longitudinal axes as defined by LV geometry (10). Myocardial motion is complex and three-dimensional, however, and attempting to quantitatively study LV dynamics unrestricted by these geometric conventions has not been done quantitatively before and could reveal a new understanding of regional dysfunction.

The established methods of regional LV strain analysis can be done using several imaging modalities. Speckle tracking echocardiography (STE) uses naturally occurring speckle patterns in the myocardium seen in ultrasound scans to assess tissue deformation (11). Cardiovascular magnetic resonance (CMR) also plays a large role in regional LV strain analysis. The CMR "tagging" method selectively magnetizes the myocardium in a grid shape at the start of the heart cycle, and follows the relative motion of the grid lines over time to quantify strain (12). CMR feature tracking (CMR-FT) is a post-processing method that tracks the motion of shapes and textures in image sequences from any cine CMR acquisition to measure deformation (13). These methods allow for regional strain measurements that can be used as a supplement to LV EF to determine earlier if and where a patient is developing cardiac diseases, such as HF, and to more confidently determine if they would benefit from treatment (14).

The methods mentioned above have all been used successfully in research and clinical applications, but all of the strain and strain rate data were presented in the context of conventional LV geometry. An alternative CMR method has been shown to be capable of producing discrete measurements of deformation magnitude and direction on voxel-scale through the application of strain rate tensors on time dependent velocity fields from phase contrast MRI (PC-MRI), although this method has never been applied on hearts with MI or in quantitative deformation analysis of the LV (15).

The aim of this thesis is to apply strain rate tensor analysis on MR data of rat hearts to study the effects of MI on regional LV dysfunction after infarct. To do this we will first prove that this method is a viable tool to measure cardiac deformation parameters by comparing global strain rate and strain measurements to literature. Different LV segmentation models will be used to look at regional variation in 2D cross-sectional and 3D whole-LV data. We will also make use of the strain rate tensor's unique properties to study the direction of strain rate in 2D and 3D and attempt to parametrize this in a way that describes myocardial function. To study change over time, we will analyze TPM MRI scans of infarcted rat heart LVs and observe how the different measurements progress over weeks after infarct compared to a healthy control group. Using this analysis framework, we will attempt to gain new insight into the dynamics of how myocardial dysfunction develops as the infarcted regions grow.

Chapter 2

Theory

This chapter introduces some fundamental MR theory, heart physiology and the mathematics of strain rate tensor calculation.

2.1 MR theory overview

In this section we will establish a basic theoretical foundation of the physics behind MRI, based on the compendium "Physics of MR imaging" from the FYS4740 course at the University of Oslo (16).

2.1.1 The spin

The most prominent atom in the human body is the hydrogen, found in water molecules and many others. The nucleus of a hydrogen atom is a single proton, and for the sake of simplicity we will imagine the human body as a heterogeneous collection of protons where different tissues have different densities.

In an MRI, a voxel contains signals that are generated from the protons within it. To understand how this signal is produced and measured, it is useful to think of the protons as spinning magnetic dipoles. More precisely, we say that these dipoles "precess" around the static B_0 -field from the MRI magnet at the Larmor frequency:

$$\omega_0 = \gamma B_0, \quad (2.1)$$

which is proportional to the B_0 field strength, where γ is the gyromagnetic ratio defined by the material or tissue. We refer to these dipoles as "spins". Other nuclei with an odd number amount of protons also have a spin property, but hydrogen has a higher γ . This makes it easier to detect, which further supports our simplification that living tissue is a collection of protons. The precessing motion is illustrated in Figure 2.1C.

When an object is placed within the magnet it does not initially produce an interpretable

signal. At this point in time, each spin in a voxel precess either parallel or anti-parallel with the \vec{B}_0 field direction. Opposite direction spins cancel out, and we end up with a vector sum pointing parallel, which represents the Net magnetization vector \vec{M} as illustrated in Figure 2.1. As long as \vec{M} points parallel to the field, we consider it to be in an equilibrium position. We can generate an MR signal by disturbing this rest state.

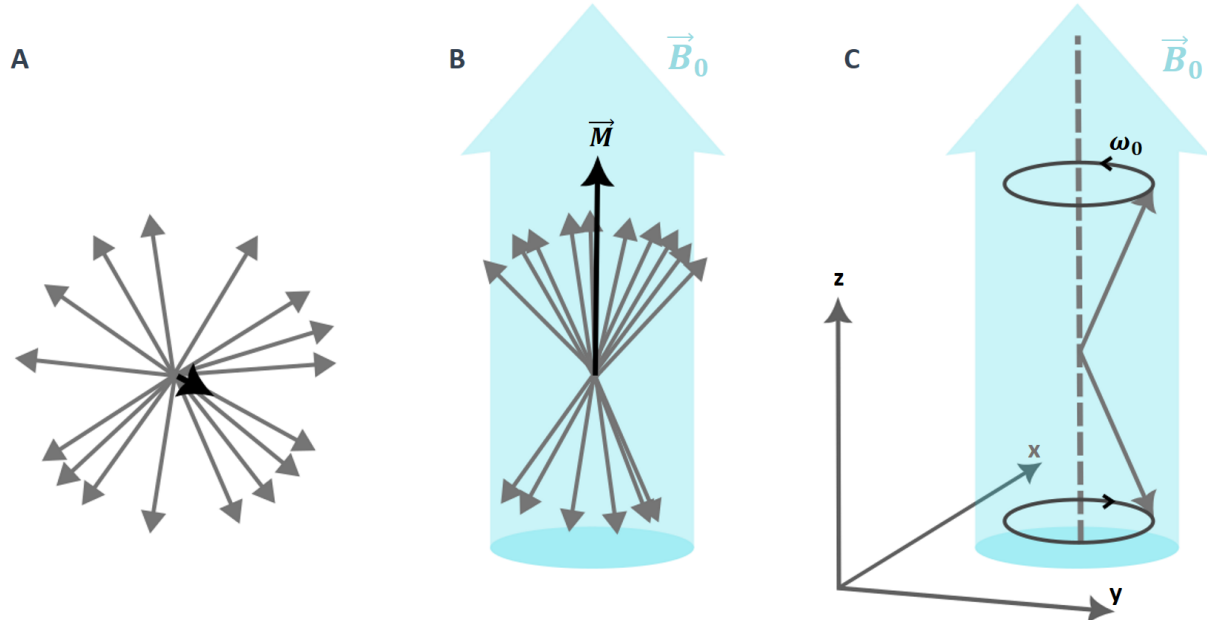


Figure 2.1: A: A group of spins pointing in random directions, with no meaningful vector sum. B: The same spins with a magnetic field \vec{B}_0 applied, creating a parallel net magnetization vector \vec{M} shown here in its equilibrium position. C: Constituent parallel and anti-parallel spins precessing around \vec{B}_0 at the Larmor frequency ω_0 .

2.1.2 RF pulse

Using an orthogonal second field \vec{B}_1 to knock \vec{M} out of its equilibrium is what leads us to the signal we need. This field alternates directions at a rate of ω_0 to effectively move \vec{M} without having to overpower the strong \vec{B}_0 field. As \vec{M} is moved down at some angle and its composite spins precess in phase, what separates signal from different tissues is how it recovers back to the rest state via two types of "relaxation". $T1$ relaxation is measured by the time it takes for \vec{M} to become parallel to \vec{B}_0 again, and $T2$ relaxation depends on the time it takes for the spins to move out of phase again. An MRI can be $T1$ or $T2$ weighted, depending on the anatomy and type of tissue we are interested in (cite??). Figure 2.2 demonstrates how the relaxation of \vec{M} generates a signal that can be measured by a magnetically sensitive receiver coil.

In the figure, $M_{\perp}(t)$ is the measured transverse component of the MR signal from \vec{M} , representing one group of spins with the same Larmor frequency ω_0 . In an MRI acquisition, however, the signal will be far more complex because it measures signal from all tissue that is magnetized by the \vec{B}_1 field.

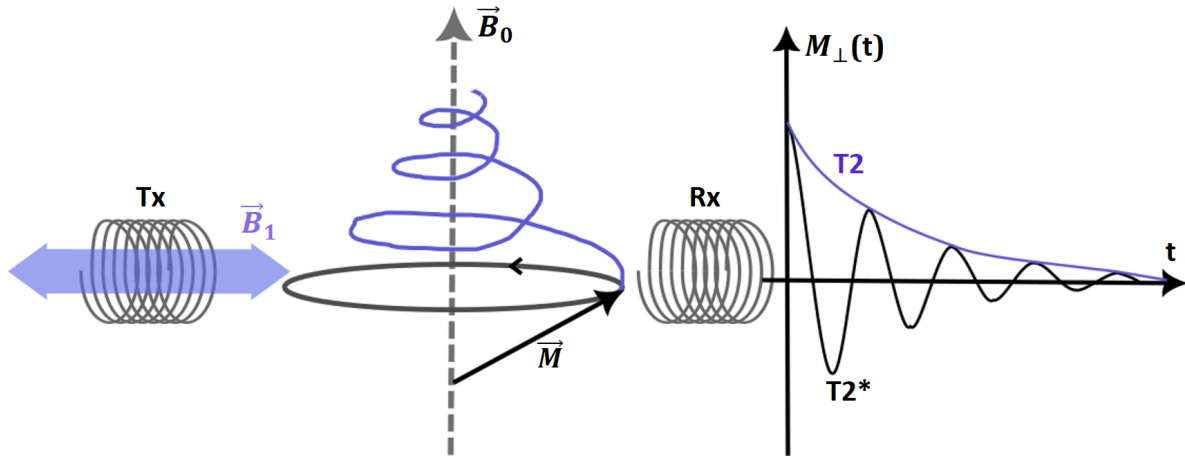


Figure 2.2: A transmitter coil (Tx) creates RF pulses that generate an alternating \vec{B}_1 field that moves \vec{M} out of its equilibrium position at some flip angle. The receiver coil (Rx) measures the RF signal generated as the flipped \vec{M} precesses and gradually regains its equilibrium. The orthogonal component $M_{\perp}(t)$ approaches zero over time as \vec{M} becomes parallel with \vec{B}_0 again.

2.1.3 Fourier transform

When interpreting the signal, we are interested in the different frequencies it contains. These tell

To be able to distinguish MR signal frequencies at different positions in a slice, a position dependent Larmor frequency is introduced via a linear gradient $\omega_{local} = \omega_0 + \Delta\omega(r)$... (to localize MR signals)

(eddy currents, potential sources of noise in signal?)

2.1.4 K-space

The image quality, contrast and precise details, depends on the amount of MRI signal sampled. H (..rewrite)

Figure 2.3 demonstrates

2.1.5 Pulse sequences

2.1.6 Motion encoded MRI / PC-MRI

(venc)

2.1.7 MRI geometry

(gantry, isocenter, fase-gradient?)

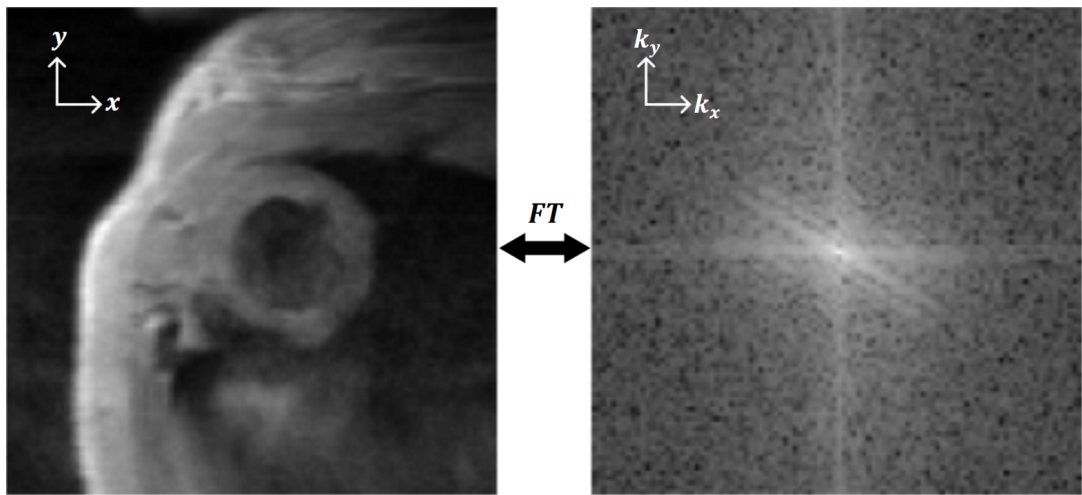


Figure 2.3: An image with pixel elements in x and y positions, and a corresponding k -space representation with the same dimensions calculated via Fourier transform. The zero frequency component ($k_x, k_y = 0$) has been shifted to the middle of the image.

2.2 Heart physiology

To interpret the data we will be using and the results we get, it is essential to have a fundamental understanding of the heart. We will take a quick dive into anatomy, physiology as well as look at deformation through strain and strain rate measurements of the LV and what these can tell us about regional myocardial function and HF.

2.2.1 Heart anatomy and the cardiac cycle

Mammal hearts have four chambers that hold and transport blood at different points in the cardiac cycle. The right atrium (RA) and right ventricle (RV) pump oxygen-poor blood to the lungs, and the left atrium (LA) and left ventricle (LV) pump oxygenated blood out into the body (17). The heart interior with labelled chambers are illustrated in Figure 2.4.

The chamber walls consist of muscle tissue called the "myocardium", which receives electrical signals that determine heart rate by triggering contracting motions that cause the pumping motions. These contracting and relaxing motions make the pulmonary valves open and close periodically each cycle to regulate blood flow from the atria to the ventricles (18). The LV is the largest of the chambers, has the thickest chamber walls and is relatively symmetrical and cone shaped (cite?). These traits make it optimal for analysis and geometrical modelling.

Going through the various phases of the cardiac cycle, we know when and how the LV myocardium should contract and relax in detail (19). The phase of the the cardiac cycle where the LV begins to contract, is called the "systole". While contracting, the LV myocardium thickens and shortens to shrink the chamber volume and pump the blood contents out into the body. We say that the wall thickens the circumference and height is shortened as illustrated in Figure 2.5. At the start of the diastole phase, the muscle

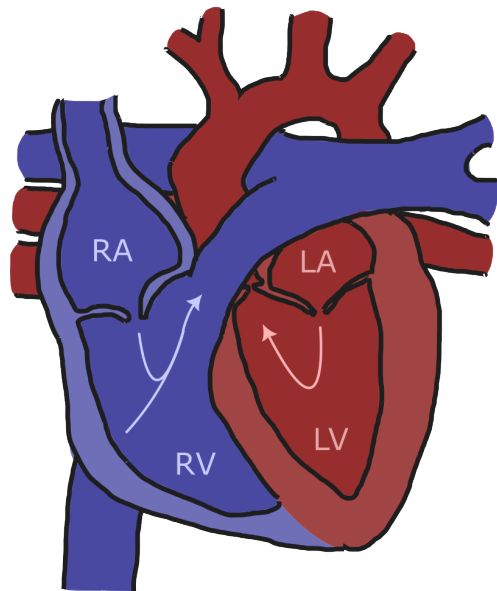


Figure 2.4: Illustrated heart interior with labelled chambers, blue indicating de-oxygenated blood and red oxygenated. Direction of blood flow through chambers indicated with arrows. Atria and ventricles are separated by pulmonary valves. The chamber walls are the myocardium.

tissue relaxes and the LV moves back to its initial dimensions, starting a new cardiac cycle.

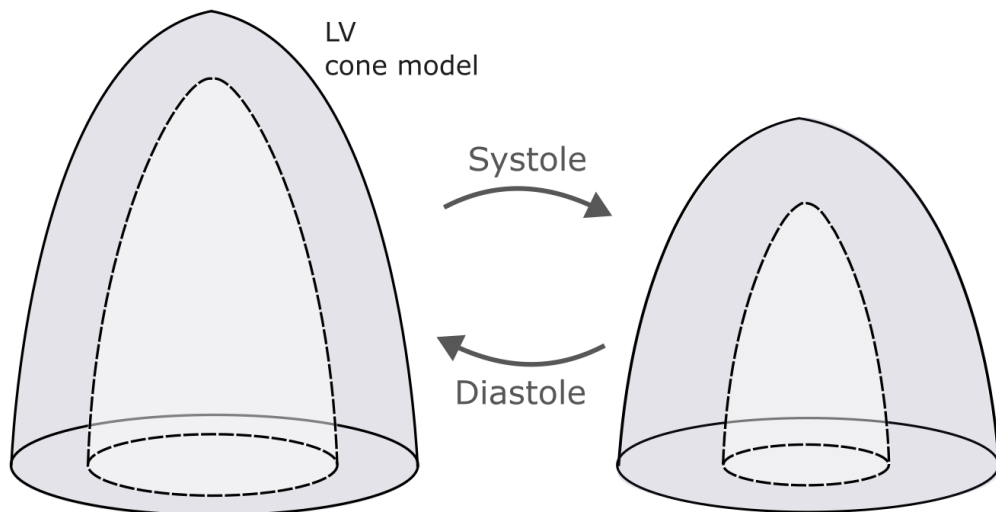


Figure 2.5: Illustration of the LV simplified as a cone, demonstrating how the myocardium thickens radially as well as reducing its circumference and length when contracting during systole to minimize the LV chamber volume. Relaxing the muscle during the diastole returns the LV to its initial dimensions and the beginning of the cardiac cycle.

(what do we mean by 'myocardial function'?)

(radial, circumferential, longitudinal?)

2.2.2 Myocardial infarction

Reduced blood flow to the myocardium, due to blockage of the atria delivering blood to the muscle tissue or other reasons, can result in a heart attack or "myocardial infarction" (MI). The tissue that lacks blood will get permanently damaged or die if blood flow is not restored. This can reduce or in the worst case completely disrupt the blood flow from the heart chambers to the rest of the body (5).

Infarcted tissue can be detected in CMR images via Late Gadolinium Enhancement (LGE), as demonstrated in Figure 2.6. Gadolinium contrast accumulates in infarcted tissue due to slow washout compared to the functional myocardium, creating a highlighting effect by causing a shortening of T1-decay. The highlight is therefore visible in T1 weighted images (20). The figure also demonstrates that the brighter section of the LV is thinner, which is another way we can identify infarction.

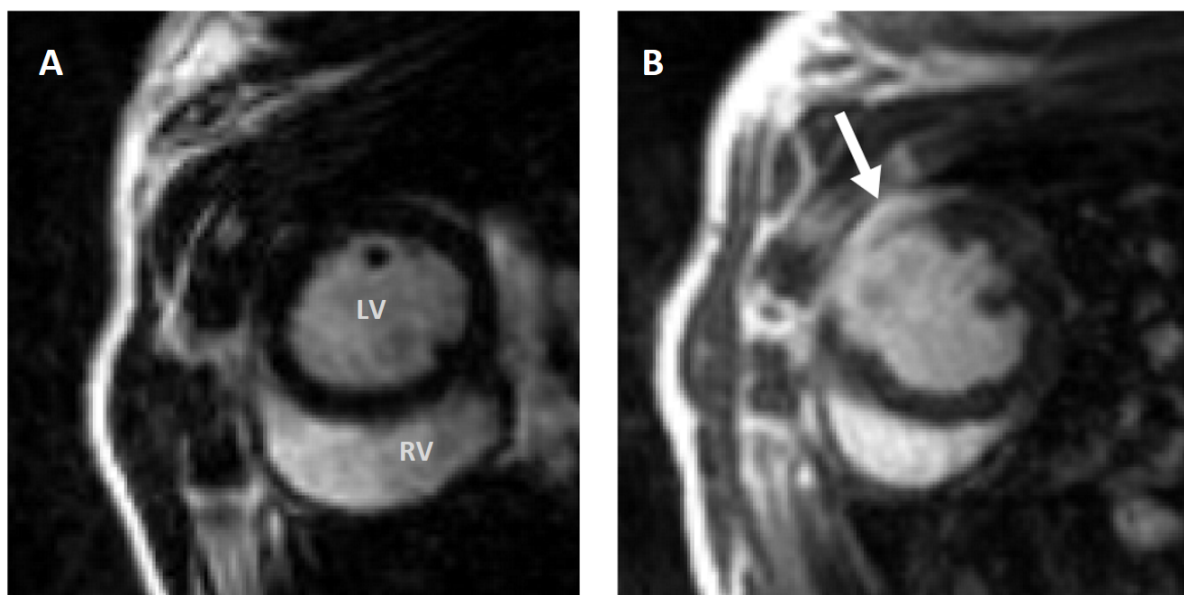


Figure 2.6: A: Sample LGE image of a Sham heart, with black LV myocardium that indicates viable muscle tissue. B: Sample LGE image of an MI heart, with highlighted infarct tissue in the LV myocardium.

Another known characteristic of the infarct tissue that results from MI is that it becomes "stiff" and gradually loses its ability to actively deform as the infarct grows (21). The heart responds to this loss of function by adjusting its mechanical properties to maintain the blood pumping capabilities of its chambers, which relates to a process called "cardiac remodelling" (22). Despite being an attempt by the body to regain function and control, the effects of cardiac remodelling themselves can cause hurtful symptoms and are clear indicators of myocardial dysfunction. These details about the mechanical dysfunction of the myocardium can be revealed by analysis of regional LV deformation, which is where myocardial strain as a functional parameter comes in.

2.3 Strain and strain rate analysis

The simple, one-dimensional definition of strain is that it is a measurement of the relative deformation ΔL of the initial length L of an object at a time point t :

$$\varepsilon(t) = \frac{\Delta L}{L}. \quad (2.2)$$

This is the Lagrangian, or "material", definition of strain (8) and is illustrated in Figure 2.7 with a cylinder that is stretched and compressed by a force \vec{F} as examples of positive and negative value strain. Strain values are expressed as a percentage % change from an initial length. What is also apparent in this figure is that the cylinders don't just deform vertically despite being affected by a vertical force, but they also deform horizontally. This illustrates the deformation of an incompressible material, which we assume muscle tissue is (23), meaning that it needs to deform in this way to conserve its mass. It should not, for example, expand in all directions or be compressed in all directions. This principle of conservation of mass in multi-dimensional deformation will be relevant again later, as we are specifically interested in deformation in two- and three-dimensional velocity fields. Strain *rate* refers to the rate of which the deformations happens, expressed with the unit s^{-1} .

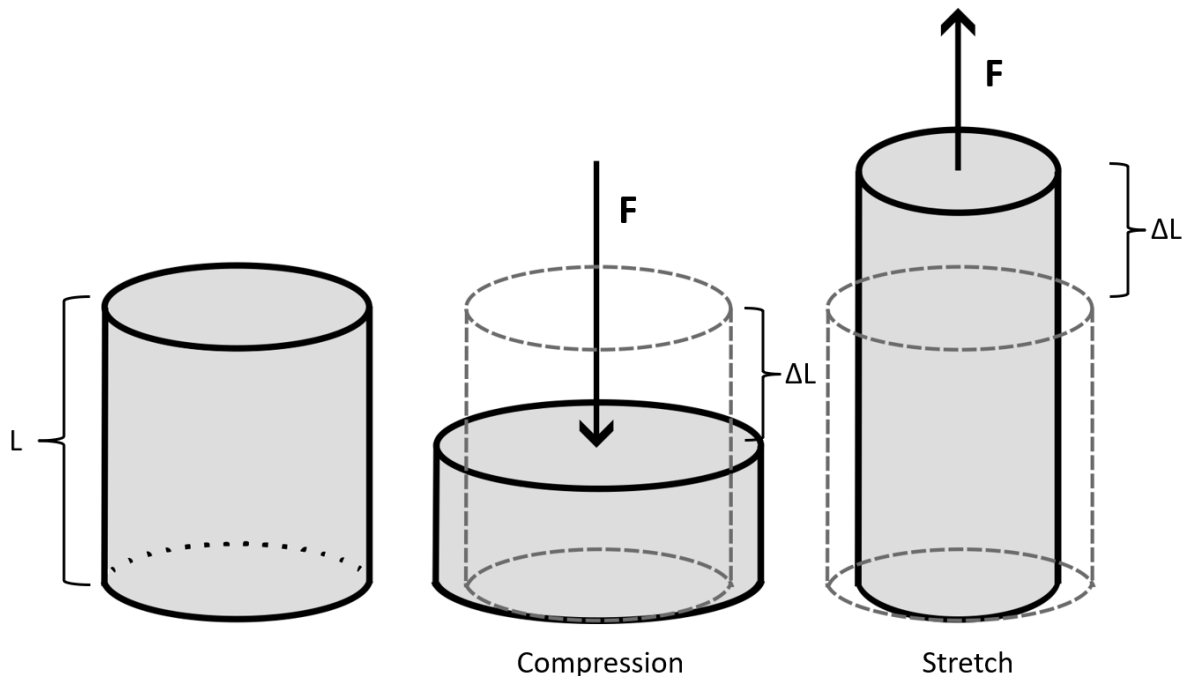


Figure 2.7: Demonstration of the one-dimensional strain ε of a cylinder of initial length L , made of an incompressible material. When the cylinder is compressed (negative ΔL) by a vertical force \vec{F} it is affected by negative strain in that direction, when it is stretched (positive ΔL) it is affected by positive strain. Illustrated horizontal deformation of the cylinder hints at strain in two/three dimensions and conservation of mass.

Figure 2.8 illustrates two different ways of calculating strain from velocity fields in

the myocardium. Using numerical integration to simulate the path of a point in the muscle tissue throughout the cardiac cycle, you can calculate displacement from an initial position over time. Spatial derivation of the displacement gives strain over time (8).

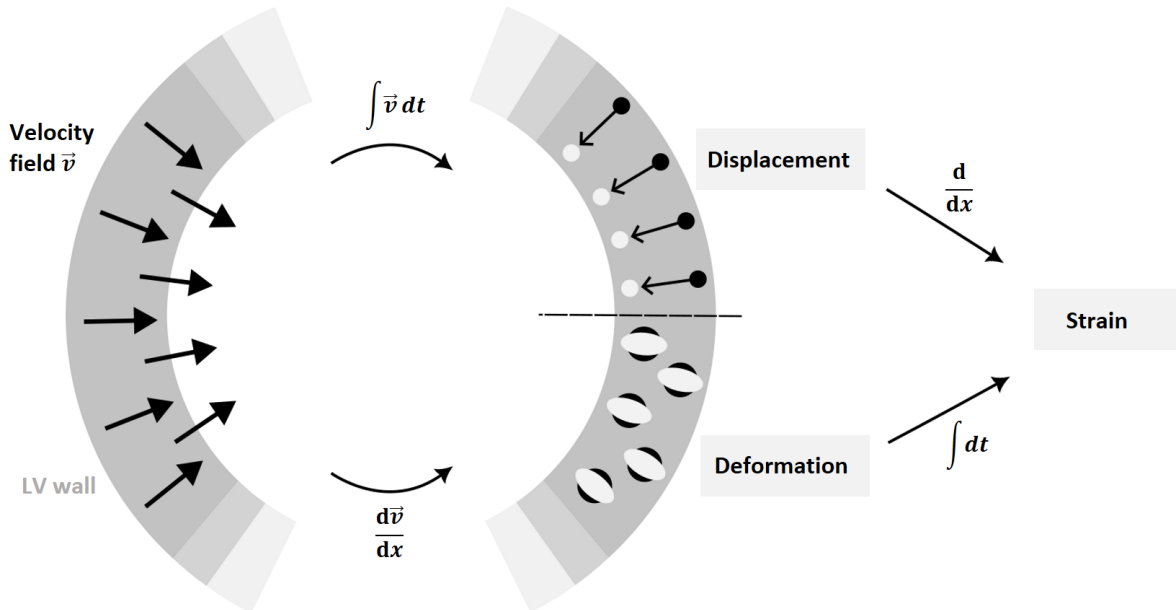


Figure 2.8: Illustration of two different methods of calculating strain from a velocity field, exemplified in LV segments here with a field describing movement of the myocardium toward the LV center. Motion tracking by integrating velocity data in time ($\int \vec{v} dt$) describes displacement of points from an initial position. Spatial velocity gradients ($d\vec{v}/dx$) describes deformation in the velocity field, illustrated as circles being deformed (stretched and compressed) into elliptic shapes.

The other alternative, the method used in this thesis, involves first applying spatial derivation to the velocity field to calculate strain rate, and then integrate in time to get strain. Spatial variation in velocities, how the tissue in one voxel moves in relation to its neighbors, describes local deformation. A mathematical method of calculating strain rate tensors from PC-MRI velocity data has been established, which we will refer to as the "Selskog method" based on the first author of the study (15). This method will be the mathematical cornerstone of our analysis, and the essential equations will be introduced in the following paragraphs.

The strain rate tensor is calculated using gradients of all velocity components all spatial axes in the relevant system of analysis. The n-dimensional velocity gradient tensor ($n \times n$ Jacobian) is calculated like this:

$$L_{ij} = \frac{\partial u_i}{\partial x_j}, \quad (2.3)$$

where $u_i, i = 1, \dots, n$ are the velocity components in the x_j direction $j = 1, \dots, n$.

Using the velocity gradient tensor, the strain rate tensor can be calculated like this:

$$D_{ij} = \frac{1}{2} \left(\frac{\partial u_i}{\partial x_j} + \frac{\partial u_j}{\partial x_i} \right) = \frac{1}{2} (L_{ij} + L_{ij}^T). \quad (2.4)$$

The eigenvalues λ_i and eigenvectors \vec{v}_i of D_{ij} are the principal values and the principal directions of strain-rate in the myocardium, as shown in Figure 2.9. The sign of the eigenvalue distinguishes between stretching (positive) and compression (negative) in the direction of the corresponding eigenvector.

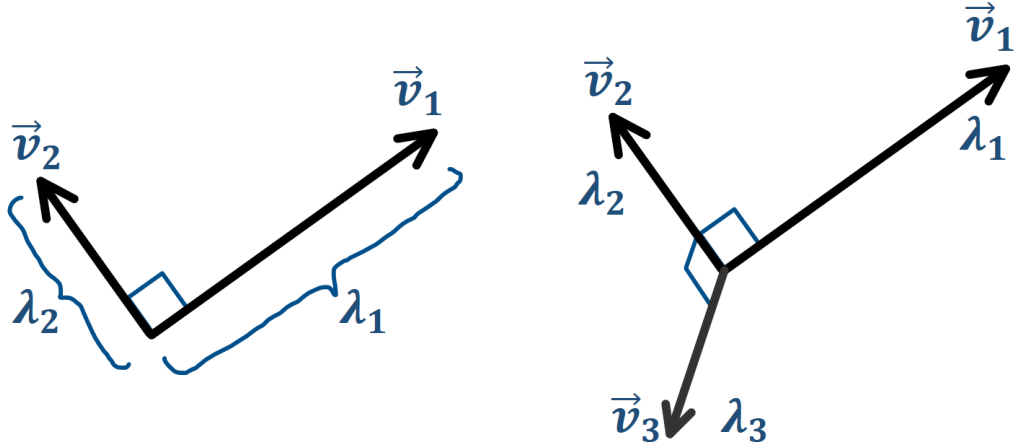


Figure 2.9: (remake?) Orthogonal eigenvectors \vec{v}_i for a two-dimensional and three-dimensional strain rate tensor D_{ij} ($n = 2$, $n = 3$), where the eigenvalues $|\lambda_i|$ represent the vector magnitudes.

The invariant I represents the total amount of strain rate in an n-dimensional strain rate tensor, irrespective of direction:

$$I = \sum_{i=1}^n \lambda_i^2. \quad (2.5)$$

Chapter 3

Material and Methods

This chapter will cover the details of the acquisition of our data, LV segmentation models, preparation for analysis and our methods of analysis including the development of our Python framework. A supplementary GitHub repository contains all python scripts developed for this thesis https://github.com/lassetotl/Thesis_CMRI_EMR.

3.1 Data overview

Here we present a short overview of the PC-MRI data that this thesis is based on. All data used was produced by the Sjaastad group at IEMR in 2017-2018, who have already used the same data in a study (24). The specifics are presented mostly the same here, with some adjustments to the study population and acquisition times.

3.1.1 Rat MI model

Male Wistar-Hannover rats (≈ 300 g) were anesthetized (96% O₂, and 4% isoflurane) and ventilated by endotracheal intubation using a Zoovent ventilator. Of the rats included in our analysis, LV MI was induced in 7 of them by proximal ligation of the left coronary artery during maintained anesthesia (98% O₂, and 1.5-2.5% isoflurane). The placement of the ligation was deliberately varied to achieve variable infarct sizes. A Sham-operated control group consisting of 6 rats underwent the same procedure with the exception of ligation. All experimental protocols were approved by the Norwegian National Animal Research Authority and performed in accordance with the European Directive 2010/63/EU and institutional guidelines (ID 3284).

3.1.2 MRI Acquisition

In time intervals after operation (1, 3, 10, 21 and 42 days), MRI experiments were performed on a 9.4T magnetic resonance system (Agilent Technologies, Inc) using hardware dedicated to rat cardiac imaging. From our selected group, we chose 23 MI datasets and 27 Sham datasets. For analysis requiring all slices of the LV, some datasets were excluded due to missing slices or slices with distorted velocity fields (20

MI and 21 Sham datasets remaining in this case). For analysis requiring single slices, no exclusions were made.

Anesthesia was induced in a chamber using a mixture of O₂ and \approx 4.0% isoflurane and maintained during acquisition in freely breathing animals using O₂ and \approx 1.5% isoflurane. Throughout the examination, ECG, respiration, and body temperature were monitored, the latter maintained at 37.0°C by heated air. LV short-axis (SHAX) imaging planes were identified from untriggered scout images, and all subsequent acquisitions triggered at the peak of the R wave and gated for respiratory motion. In all data sets, the temporal resolution was equal to the repetition time.

PC-MRI used an RF-spoiled black blood gradient echo cine sequence using 9-point velocity-encoding (25) and rotating field of view (26). Several SHAX slices were acquired to cover the entire LV. All slices were parallel and shared a common center normal. The PC-MRI time series also covered $>100\%$ of the heart cycle. Imaging parameters were echo time TE=2.22 to 2.26 ms, repetition time TR=2.93 to 3.21 ms, field of view FOV=50x50 mm, matrix=128x128, slice thickness $\Delta z=1.5$ mm, flip angle=7°, velocity encoding strength=13.9 cm/s, signal averaging=2x using rotating field of view, total acquisition time=45 to 50 minutes.

In each PC-MRI slice, the myocardium was segmented using a semiautomatic method that requires the user to delineate the endo- and epicardium at end systole and end diastole. The masks were then automatically propagated throughout the cardiac cycle based on the underlying velocity fields. The myocardial masks were divided into 36 equal sectors defined by the LV center. The sectors that were determined to include infarcted tissue during segmenting, based on LGE MRI images, are noted in the metadata of each dataset to localize fibrosis in the analysis.

3.2 LV segmentation models

To be able to perform regional deformation analysis of the LV, we need to establish models that divide our MRI data into segments that can be measured separately to study variation. Figure 3.1A shows a segmentation model where the LV is divided to study regional variation within a single basal slice. The details of how the slice is segmented is discussed in section 3.3.7.

Figure 3.1B shows a second segmentation model consisting of a series of slices covering most of the LV, divided into a basal and apical half. It has been shown that the effects of cardiovascular disease can affect LV mechanics differently at different levels (10). The intention with our model is to also look at three-dimensional regional variation of our measured parameters. If the processed heart data contains an odd number of slices, we have chosen to include the middle slice in both the basal and apical half.

The "slices" in these models are in practice masks of the voxels in the TPM scans that contain the LV myocardium, producing quite circular shapes for images in the SHAX plane. These masks cover the LV myocardium, which contains velocity fields describing the muscle tissue motion we will analyze.

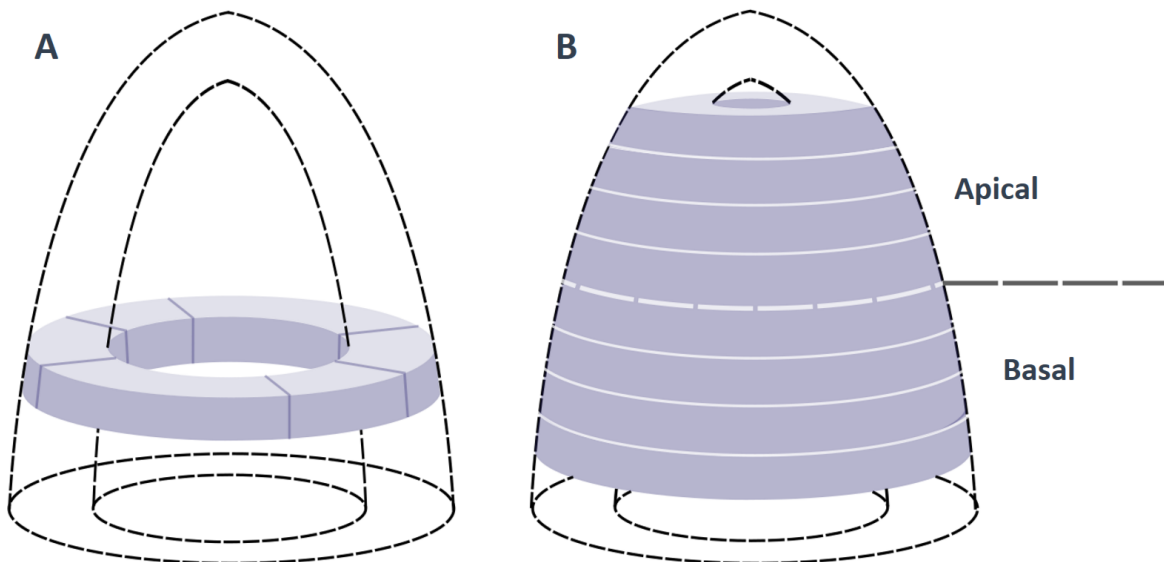


Figure 3.1: The LV segmentation models used in this thesis. A: Model that studies regional variation within one basal slice by segmenting it into separate sections. B: Model that studies regional variation in a series of slices that covers most of the LV. The stack is split in the middle into an apical and a basal group.

For our LV models we assume cylindrical geometry (27). This means that the longitudinal direction is always defined as the z-direction; orthogonal to the SHAX xy-plane. It also means that whenever we refer to an "LV center" we refer to the center of the relevant LV slice, and never the center of the entire sequence of slices.

3.3 Strain rate tensor analysis framework

This section discusses the process of how our Python framework uses the TPM SHAX velocity fields to calculate strain rate tensors in the myocardium, visualize them and analyse LV strain rate and strain globally and regionally in the radial, circumferential and longitudinal directions using 2D and 3D strain rate tensors. The framework will also be able to use the tensors to assess the direction of strain rate unrestricted by the conventional axes in heart geometry.

3.3.1 The velocity field

The TPM data is stored as a large MATLAB structure containing many different fields and parameters, which is imported to Python as a large dictionary structure.

Relevant to this framework, we have time dependent velocity fields representing cardiac motion, magnitude fields that represent proton density and relaxation dynamics. The structure also contains a binary mask matrix, designed during processing, with the same dimensions as the image with value 0 in voxels determined to be outside the myocardium and value 1 inside. Relevant static parameters are infarct sectors for MI hearts with visible infarction, slice position $pss0$ relative to the gantry isocenter and the time points at end systole T_{es} and end diastole T_{ed} .

For our analysis, only tissue in the LV is relevant and we have to exclude noisy signal from the movement of blood. This can be achieved by applying the binary mask. The velocity field inside the myocardium is also affected by noise, so we need to smooth the data to compensate for this. For this we can apply the following smoothing function to our velocity field (15):

$$u_{i,smooth} = \frac{(u_i \cdot c) * g}{c * g}, \quad (3.1)$$

where u_i is a velocity field for a spatial component i , and g is a 3D Gaussian function with a standard deviation $\sigma = 2$. Convolution is denoted with a " $*$ ". The "c" is defined as a "certainty" matrix, calculated by normalizing the magnitude field to have values in the range $c_k \in [0, 1]$ for a voxel k . The intention with the certainty values is to suppress velocity signal from the blood, as it produces lower magnitude values than soft tissue, before smoothing with the Gaussian application function. The "black blood" sequence used to acquire the TPM data further ensures that voxels with blood signal give low certainty values and lesser effect on gradient calculations later.

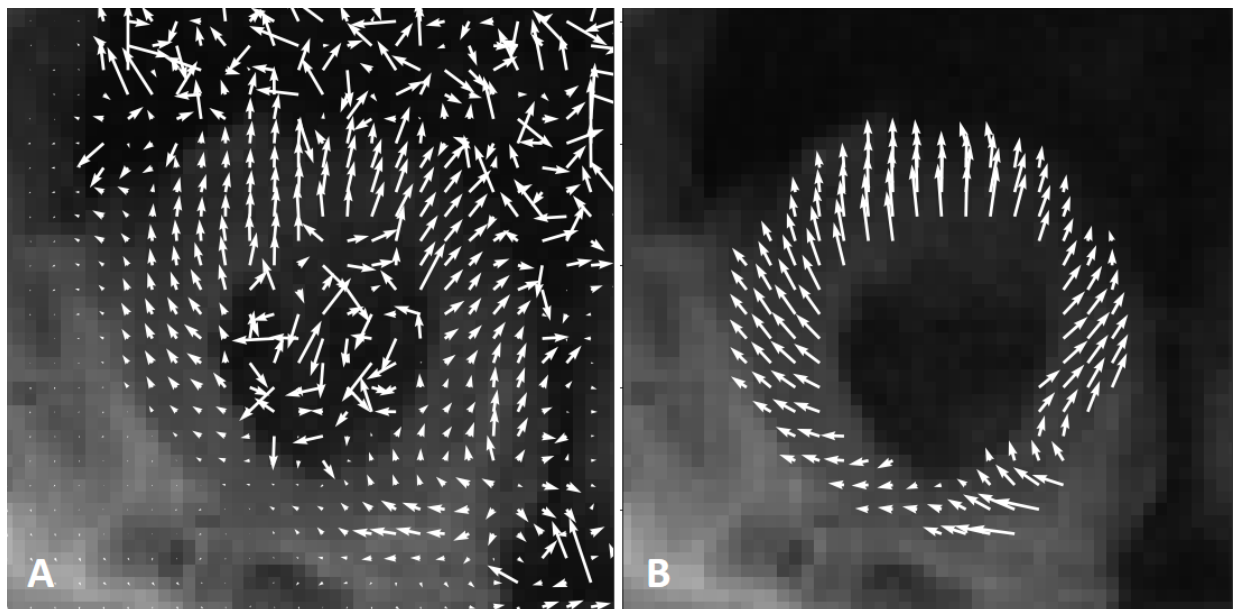


Figure 3.2: A: Velocity field \vec{u} in a 2D SHAX slice in early diastole, including noisy signal in the blood. Magnitude plot in the background. Vectors are plotted with a spacing of one voxel. B: The same field at the same time but with Equation 3.1 applied to velocity components u_x and u_y and a binary myocardium mask applied.

The effect of smoothing the velocity field and then applying the mask is demonstrated in Figure 3.2. Seeing the effect of the mask is obvious, but notice how the velocity field within the myocardium also becomes more homogenous than in the initial data as well.

3.3.2 Numeric implementation of Selskog method

With the velocity fields from our TPM data we can calculate strain rate tensors in every voxel at every time point via the Selskog method discussed in Section ???. This includes smoothing of the velocity fields prior to any calculations to limit the effect of noise on gradient calculations. A numerical implementation of the velocity gradient, weighted by certainty values, is defined like this (15):

$$\frac{\Delta u_k}{\Delta x} = \frac{c_{k+1}(u_{k+1} - u_k) + c_{k-1}(u_k - u_{k-1})}{\Delta x(c_{k+1} + c_{k-1})}, \quad (3.2)$$

where Δx is the resolution in the direction of the gradient and u_k and c_k are the velocity and certainty in a voxel k . To calculate the strain rate tensor D_{ij} (Equation 2.4) in voxel k in a cartesian 3D velocity field, we need this 3×3 gradient tensor L_{ij} via Equation 2.3:

$$L_{ij} = \begin{bmatrix} \frac{\Delta v_x}{\Delta x} & \frac{\Delta v_x}{\Delta y} & \frac{\Delta v_x}{\Delta z} \\ \frac{\Delta v_y}{\Delta x} & \frac{\Delta v_y}{\Delta y} & \frac{\Delta v_y}{\Delta z} \\ \frac{\Delta v_z}{\Delta x} & \frac{\Delta v_z}{\Delta y} & \frac{\Delta v_z}{\Delta z} \end{bmatrix}, \quad (3.3)$$

where the x- and y-directions are in the SHAX plane and the z-direction is orthogonal and out of plane (longitudinal direction). For a 2×2 gradient tensor from a 2D field, we simply get:

$$L_{ij} = \begin{bmatrix} \frac{\Delta v_x}{\Delta x} & \frac{\Delta v_x}{\Delta y} \\ \frac{\Delta v_y}{\Delta x} & \frac{\Delta v_y}{\Delta y} \end{bmatrix}. \quad (3.4)$$

To get correct gradient values we need to take into account the voxel dimensions in the TPM data, which is especially important in 3D because $\Delta x = \Delta y \neq \Delta z$. From the metadata we find that the slice thickness is $\Delta z = 1.5mm$, while the in-plane voxel resolution is $\Delta x = \Delta y \approx 0.35mm$.

When we apply masks to the velocity fields we exclude voxels that were determined to be outside the myocardium, but the mask borders may still be an issue when calculating gradients. When the strain rate tensor is calculated in a voxel, the gradients require velocity values in adjacent voxels in the gradient direction (as seen in Equation 3.2). If the voxel is positioned right at the edge, one of its neighbors could be outside the mask and distort the gradient value because it contains noisy signal from the blood.

Noise contamination is supposedly compensated for when using Equation 3.1 to smooth the velocity field, but we can also choose to exclude the outermost voxels by performing a "binary erosion" of the mask to avoid the issue altogether. This shaves off a layer of voxels on the inside and outside edges and ensures that all in-plane gradient

calculations are performed completely within the mask. This is demonstrated in Figure 3.3.

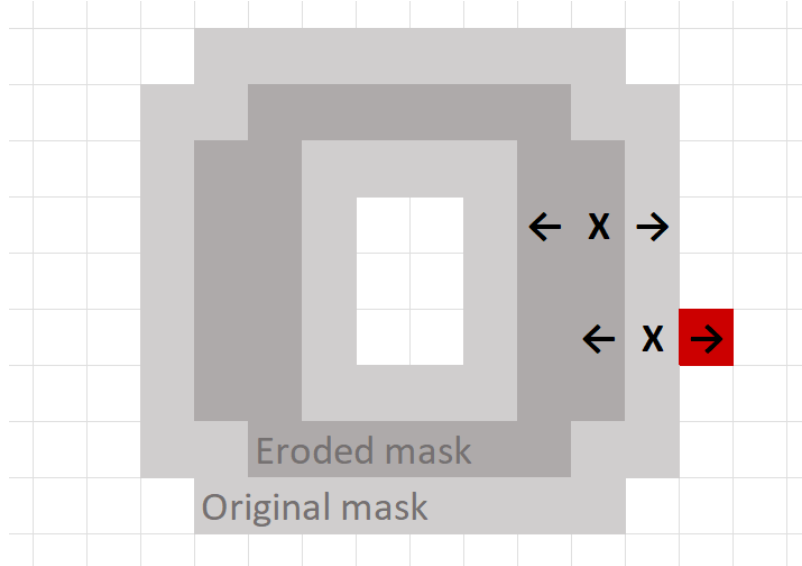


Figure 3.3: A demonstration of binary erosion. For any sampled voxel ("X") in the eroded mask, it will always have neighbors inside the original mask.

This could, however, mean that we sacrifice data along the epi- and endocardium that is valuable in LV deformation analysis, especially longitudinal strain (28). We will investigate if the smoothing function sufficiently counters border artifacts, and apply binary erosion if not to more directly prevent blood signal contamination.

Blood signal is especially an issue when calculating gradients in the z-direction. In this case the gradients require velocity values in the slices above and below, and as the radius of the LV masks vary in different positions we hit a lot of zeroes outside the masks. We solve this by applying a "Nearest Neighbor" function, where the framework finds the nearest non-zero value and uses that instead. This leads it to find velocity data in the myocardium nearby.

3.3.3 Ellipsoid tensor visualization

We now have the tools to calculate strain rate tensors in each voxel of the myocardium for every frame over a full heart cycle, using processed velocity fields. To interpret these tensors, it is useful to visualize them in a way that intuitively communicates their direction and magnitude of strain rate.

The eigenvectors of the tensor are always orthogonal to each other, and we can use them to span the half-axes of an ellipsoid, or in the two-dimensional case: simply an ellipse (15). The ellipse shape is intended to deform according to the strain rate direction and magnitude that corresponds to its half-axes, meaning that it should expand along the axis where we have stretching (positive eigenvalues) and contract along the axis with compression (negative eigenvalues) or have a roughly spherical shape when the magnitude is around zero.

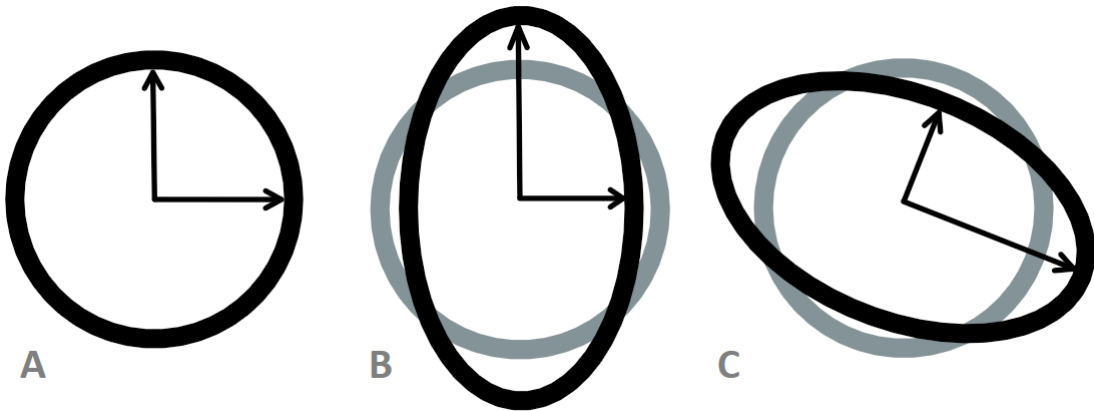


Figure 3.4: Ellipses spanned by eigenvectors of various directions, vector lengths modulated by eigenvalues. A: magnitudes around zero; no deformation gives a circular shape. B, C: Stretch and compression give elliptic shapes.

A circular shape could also represent a tensor that either expands or contracts equally along both half-axes. We expect, however, to see compression along one eigenvector and expansion along the other for the majority of 2D strain rate tensors due to the assumption of the heart tissue being incompressible and assuming conservation of mass.

To visualize the tensors as these ellipses, we transform the magnitudes to force the eigenvalues to be positive definite (29). In other words, all positive and negative eigenvalues are transformed to some positive value relative to the unit circle radius of 1. We have chosen to use the function $w(\lambda_i) = \tanh(\lambda_i) + 1$ where λ_i is some eigenvalue. This transforms the half-axes with positive eigenvalues to have lengths in the range $w \in (1.0, 2.0)$, the negative values to have values in the range $w \in (0.0, 1.0)$ and ensures that $w(0) = 1$. Letting the eigenvector pairs with transformed lengths $w(\lambda_i)$ span ellipses gives us the desired visuals in Figure 3.4.

Keep in mind that this function is only applied as a *visual* tool for the ellipse plotting, and not in the quantitative analysis. This means that the constants above are somewhat arbitrary and could be scaled later for visibility, but the point is that it produces the correct ellipse proportions and normalizes the scale to make the low magnitude tensors clearly visible. The same principle goes for 3D strain rate tensors too, but with an ellipsoid spanned by three orthogonal eigenvectors.

To more effectively communicate the regional variation in strain rate direction and magnitude visually, we can choose different parameters to assign to a color range and to the opacity of the ellipses. One such parameter, from assessing the direction of some tensor in the myocardium, is the angle θ_i of the eigenvectors relative to radial direction as defined in Figure 3.5.

Here we also demonstrate that the alignment of the ellipse relative to the radial and circumferential (tangential) axes determines strain rate direction. In other words, if you flip any of the eigenvectors 180° they still correctly describe the direction. Because the LV moves and deforms from its initial position and shape, we need to calculate the LV center position for every frame to ensure that this geometric model is consistent.

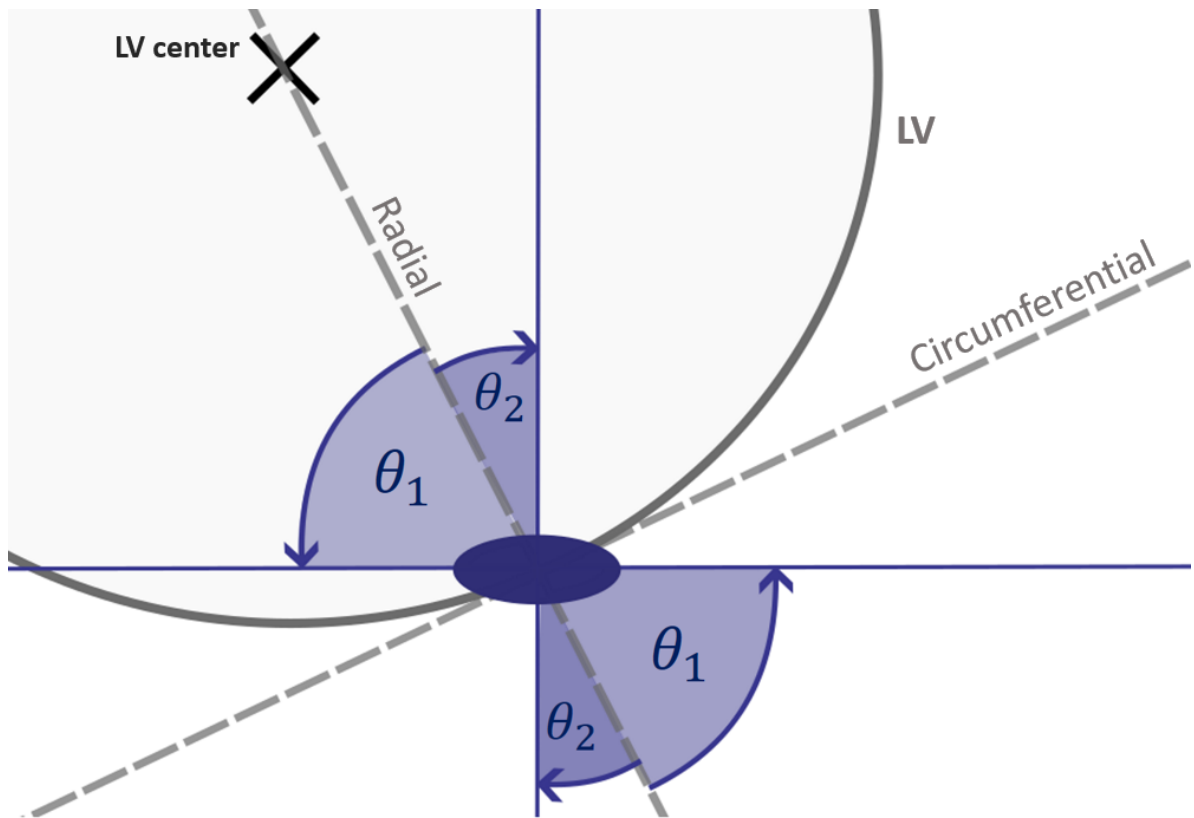


Figure 3.5: Diagram of an ellipse positioned in a coordinate system with radial and circumferential axes (dashed lines) defined by LV geometry and ellipse position. The ellipse half-axes, representing the tensor eigenvectors \bar{v}_1 and \bar{v}_2 , are oriented with angles θ_1 and θ_2 with respect to the radial axis.

This means that all possible ellipse alignments in xy-space can be described by the range of a single angle $\theta_1 \in [0, 90]^\circ$, where 0° represents a completely radial alignment and 90° a circumferential alignment. θ_2 is always orthogonal to θ_1 in the xy-plane for 2D strain rate tensors. We will map the angle of each tensor's most positive strain rate (stretch) to a color scale with this range to get a visual of directional homogeneity when plotting the ellipses. The opacity will be assigned to the Invariant I via Equation 2.5, representing total strain rate magnitude, which will create a 'dimming' effect in voxels with low-magnitude strain rate values that can reveal regional dysfunction.

3.3.4 Eigenvector decomposition

The angles θ_i will not only be used for visual analysis, but will also be used to gather quantitative information. Vector decomposition, using the eigenvector angles θ_i and eigenvalues λ_i as vector length, can be used to find the radial and circumferential components r_i and c_i of the strain rate in each voxel. These components are simple to find using the trigonometric formulas for right triangles, which we can construct with the eigenvalue λ_i as the hypotenuse and r_i and c_i as the catheti. This is shown in Figure 3.6.

For a slice at some time-point in our MR recording we generally have hundreds of voxels in the LV to sample, so we need some way of organizing the data we collect

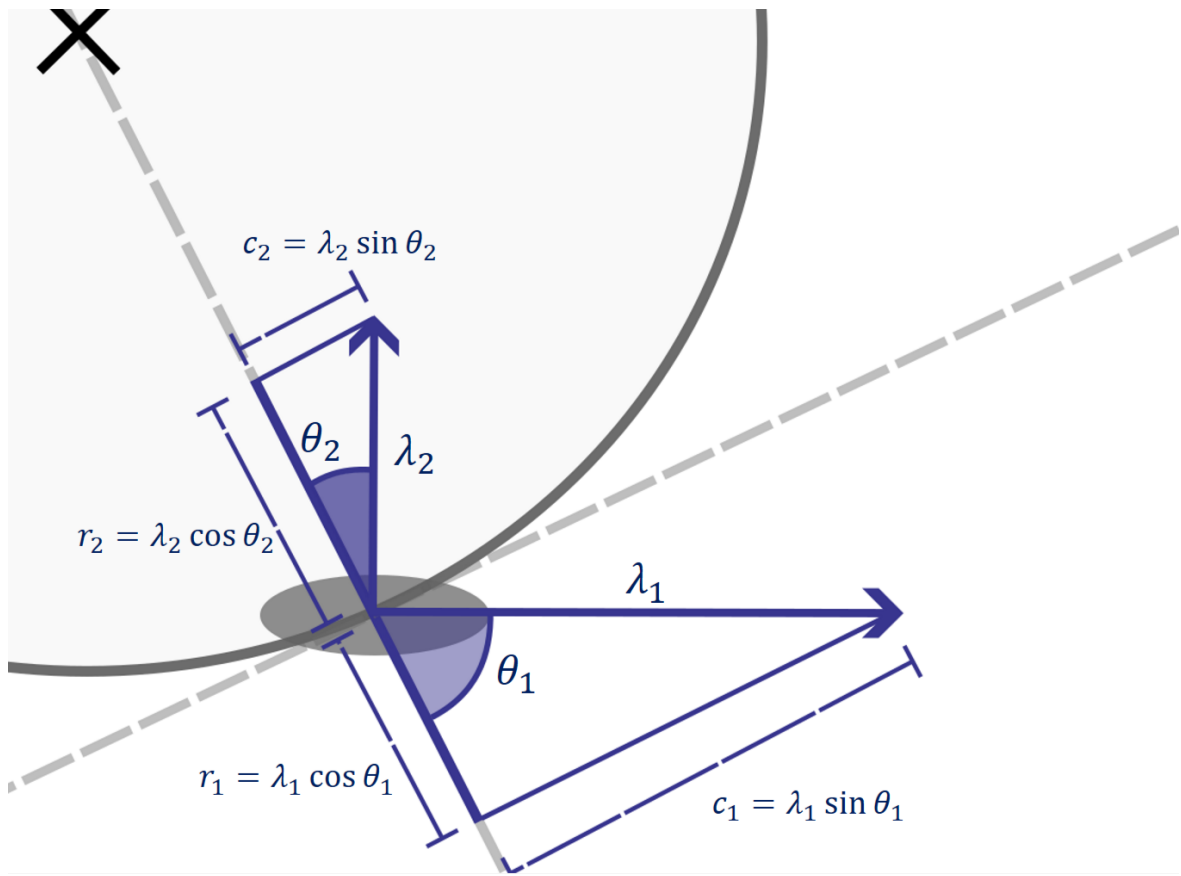


Figure 3.6: The eigenvectors represented by the ellipse in Figure 3.5 in the same coordinate system. Radial and circumferential components r_i and c_i are defined by corresponding θ_i and λ_i .

from the tensors in each of these. When using 2D strain rate tensors to analyze the voxels in the LV mask we are interested in their weighted average sum of radial and circumferential strain rate where the radial and circumferential components r_i and c_i of one tensor are calculated as shown in Figure 3.6. The weighted average sums of these components represent the global radial and circumferential strain rate for this LV slice.

3.3.5 Global LV strain rate

When plotting the global radial and circumferential strain rate for all of the time-points of velocity data in a slice from the LV base, we expect to see curves resembling the global strain rate curves as seen in (**theory section**). Whether we get a positive or negative peak depends on the sums of positive and negative eigenvalues λ_i modulated by the trigonometric functions defined by strain rate angles θ_i .

To get correct peak values, we need to make sure that the units are scaled correctly throughout the calculation process. Firstly, we need to keep count of the amount of tensors generated within the LV slice at any time point as the myocardium mask changes its shape and size throughout the cardiac cycle. Dividing the strain rate sum for this frame by this amount is how we get a weighted average measurement and also prevent larger LV cross-sections from giving a higher signal because it has more voxels in the mask. Secondly, the units of the velocity components are cm/s , and we want strain

rate measured in the unit s^{-1} which means all spatial and temporal variables should be converted to cm and s .

Previously, we have smoothed the velocity field in the SHAX xy-plane, but we have not yet smoothed our data in the time dimension. We expect the initial curves to be noisy because of this. To solve this we simply apply a running average smoothing function on the strain rate curves. The running average function convolves the curve with a kernel of length $N = 2, 4, 6\dots$ with elements $1/N$. For $N = 4$ a datapoint is transformed to the average of itself and its 4 surrounding points within the kernel, and higher kernel sizes increases the amount of smoothing.

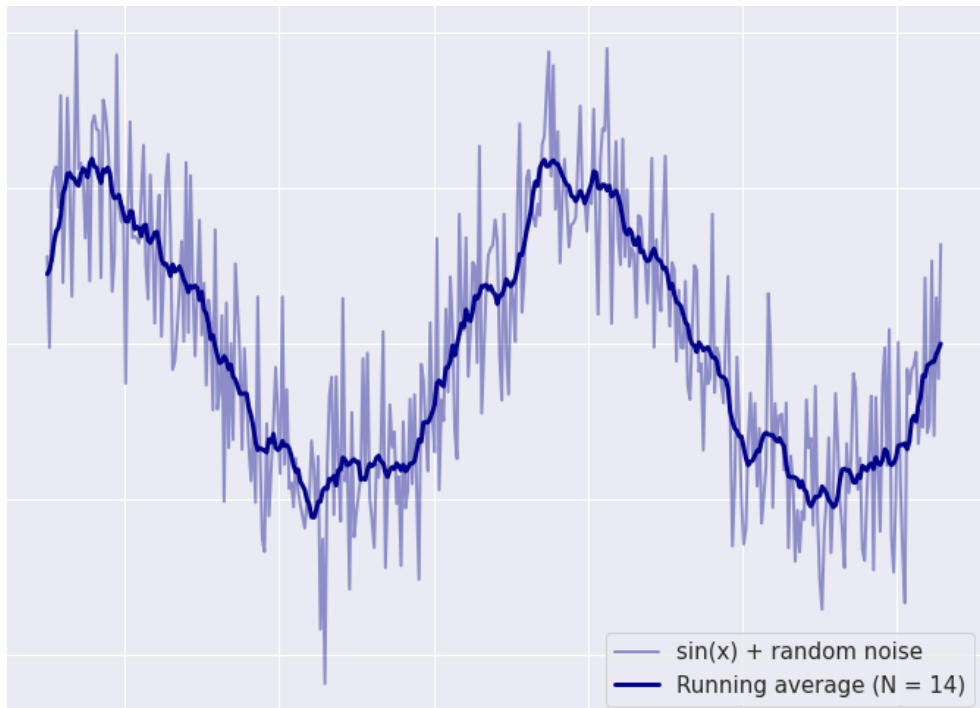


Figure 3.7: Sine signal with random noise and a curve showing the same signal smoothed by running average function using $N = 14$.

Figure 3.7 shows a simple example of the smoothing application of the running average function on a noisy sine wave. In this example we see that the smoothed curve represents an 'underlying' sine curve clearer and has more distinct peaks and valleys, but it is also worth noting that this function also essentially acts as a low-pass filter on the signal. This means that the highest signal peaks are reduced after smoothing, and we should keep in mind that higher kernel sizes N give both more smoothing and lower peaks. To minimize the chance of reducing the peak values of our 'underlying' signal, we will attempt to find a balance by finding the lowest N that gives readable and coherent curves with distinct peaks.

3.3.6 Global LV strain

From theory section 2.3 we know that we can find strain from time-integrated strain rate. In our framework we use cumulative trapezoidal numerical integration to produce strain curves from our measured strain rate data. Specifically, we use the

"`cumulative_trapezoid()`" function from the "`scipy.integrate`" module. The units will be %, representing relative deformation from the initial time-point.

Despite previously smoothing the strain rate data, the strain curves can still be affected by noise. Velocity offset in PC-MRI due to gradient eddy-currents can be a source of background noise that can accumulate during integration. This effect, in the context of cyclic motion, has been investigated in detail in a study by Pelc et al. (30).

In this study, they modelled time-dependent integrated noise to represent how the accumulated noise increases all the way to the end of a recorded time sequence. They also demonstrate that integrating both forward and backward along the timeline and using a linear combination of them both lets us minimize noise at the beginning and end of the acquisition, as shown with the combined curve in Figure 3.8B.

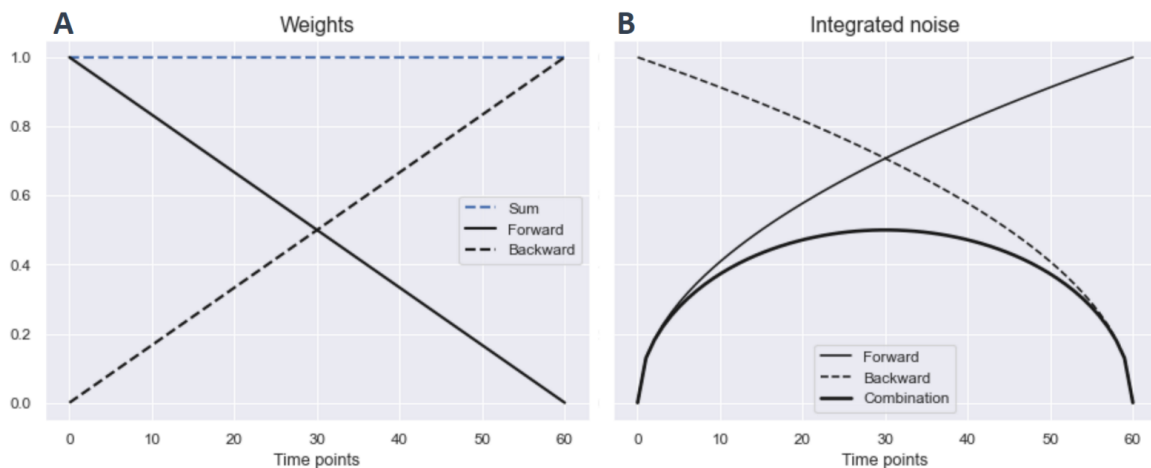


Figure 3.8: A: Linear weights designed to gradually cancel out signal at time points where integrated noise is higher. Their sum is included to illustrate that the signal is not damped or amplified by the combination. B: Mathematical models of accumulated noise from forward and backward integration, as derived by Pelc et al. Combined curve illustrates minimization of accumulated noise at both ends achieved with linear weights.

The study also suggests the application of linear weights to the forward and backward integrated curves, shown in Figure 3.8A. The sum of these weights always equals 1 to ensure that the signal is not reduced at any point, but they prioritize the integrated curve with the least accumulated noise at each time point. Both curves will be weighted equally in the middle, where accumulated noise is expected to be the same.

These principles and models will be applied in our framework. For strain curves calculated with forward integration S_f and backward integration S_b the following weights will be produced:

$$w_f = (T_{ed} - t)/T_{ed}, \quad w_b = t/T_{ed}, \quad (3.5)$$

where T_{ed} is the end diastolic time point in the relevant acquisition. The combined strain signal that we will use in the analysis can now be produced through linear combination:

$$S = w_f S_f + w_b S_b. \quad (3.6)$$

3.3.7 Regional strain and strain rate

To perform regional strain and strain rate analysis, we want to divide the LV into sections that can be analyzed separately to assess strain homogeneity. From the TPM data structure we can find time-dependent sector maps for each slice with the same dimensions as the image and velocity matrices that assign every voxel to one of 36 sectors as shown in Figure 3.9A. Infarcted hearts will also include infarct sectors in the metadata designed during processing. In the case of the figure, the metadata would contain a tuple "(1, 10)" representing an infarct sector range from 1 to 10.

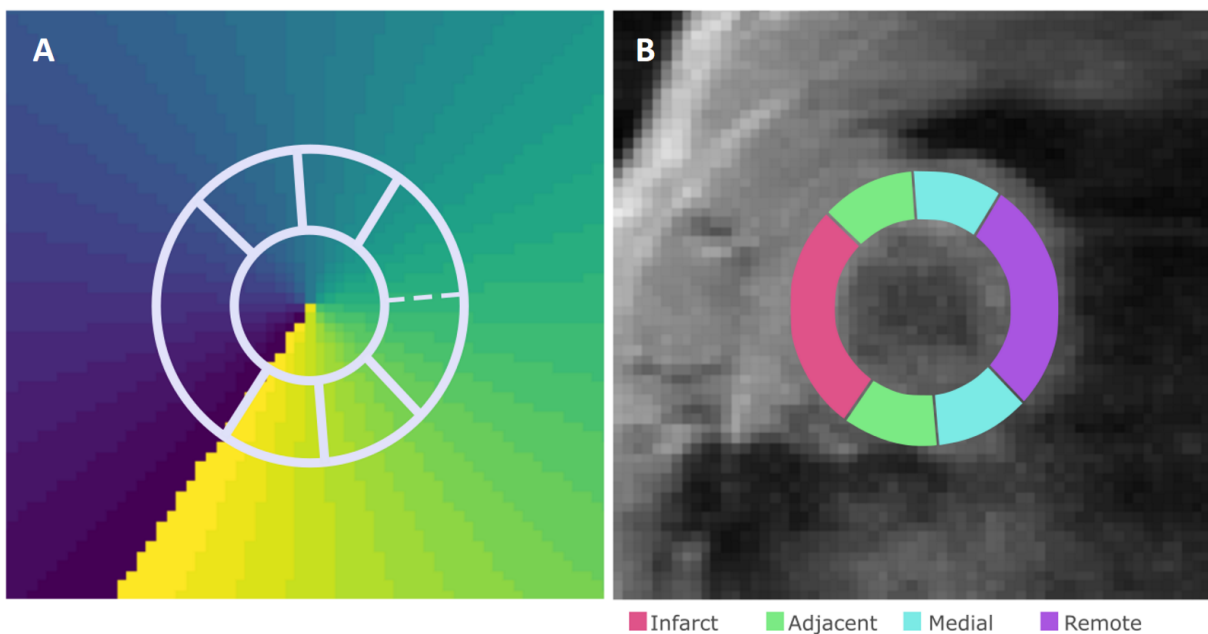


Figure 3.9: A: Sector map plotted as a clockwise color scale from sector 1 to 36, divided by isotropic lines from the LV center. Different LV sections are outlined where the largest (from sector 1 to 10) represents the infarct sectors of this heart. The rest is divided into 6 equal parts. B: The same sector groups color coded based on infarct proximity.

For the infarcted hearts, we want the infarcted sectors (as determined by the metadata) to be part of one group. The remaining LV will be split into six and distributed to three groups based on proximity to the infarct sectors: adjacent, medial, remote (31). This is shown in Figure 3.9B. If the remaining sector amount is not divisible by 6 we round down to the closest number and assign the remaining sectors to the remote group.

The Sham control group will of course not have infarct sectors, and some in the MI group as well if there was no visible infarct in the MRI LGE images. In these cases, we choose an infarct sector range approximately where we find infarction in the MI hearts and rename the groups to "Group 1" and so on. For this use we have chosen to define Group 1 by the range [4, 13] which ensures that the four groups approximately cover the same amount of sectors.

We can now perform strain and strain rate analyses like we did for the whole LV but with each of these groups separately, which lets us observe regional variation between the different sections of the LV.

3.3.8 Eigenvector angle distributions

The analysis described thus far relies on the vector decomposition of strain rate tensor eigenvectors and eigenvalues in the radial and circumferential direction in our LV model, which is conventional in LV strain analysis. However, a unique property of our tensor framework is that we can look at distributions containing tensor data on strain rate magnitude and direction for every individual voxel in the image.

We will attempt to make use of this by plotting distributions of eigenvector angles in the range $\theta_i \in [0, 90]^\circ$ relative to the radial axis over the cardiac cycle duration. We will divide the vectors into two groups based on whether they describe stretch or compression. The intent with this kind of analysis is to study how the myocardium is organized as it deforms during the cardiac cycle, regardless of the magnitude of strain rate and unrestrained by conventional LV geometry, and see if angle distribution characteristics correlate to infarct progression.

To the extent of our knowledge, this kind of analysis has not been performed before to assess heart function. This means that we need to observe these distributions for sham and MI hearts and attempt to interpret them and see if there are quantifiable differences we can establish as a parameter that reflects myocardial function. This will be discussed further in section 4.1.4.

(eigenvalue distribution Sham/MI to determine that both eigenvectors and values determine the strain rate curves?)

3.3.9 Framework adjustments for 3D analysis

We can expand our framework to include 3D strain rate tensors, which lets us perform strain analysis out of the SHAX xy-plane. This requires the introduction of the longitudinal axis and another directional parameter ϕ , as defined in Figure 3.10. We choose a cylindrical coordinate system in our 3D model, meaning that we define the longitudinal direction to always be in the z-direction and that the LV center is always defined in-plane for any slice along the LV.

The depicted ellipsoid is spanned by three orthogonal eigenvector and eigenvalue pairs as established in Theory section 2.3 that can point in any directions in 3D space, unlike the 2D tensors confined in the xy-space. We choose to describe these directions using (θ, ϕ) -coordinates, where θ relative to radial axis is defined like before and is found from in-plane projections of each eigenvector.

The in-plane angle θ can be used like before to obtain radial and circumferential components of strain rate, but now we can also find the longitudinal component simply as $l_i = \lambda_i \cos \phi_i$. When using the 3D tensors, the framework will also collect directional pa-

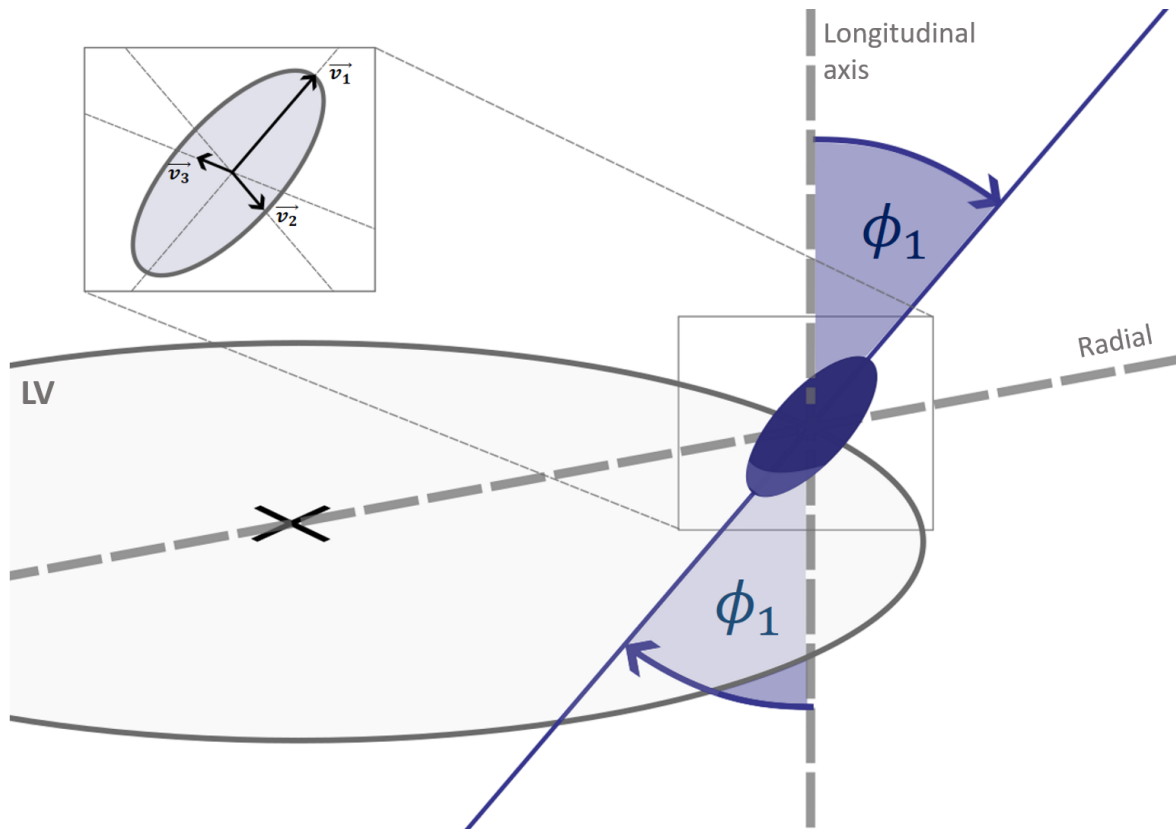


Figure 3.10: 3D strain rate tensor ellipsoid placed in LV coordinate system, where its most positive eigenvector \vec{v}_1 has an angle ϕ_1 relative to the longitudinal axis.

rameters with ϕ values in the range $\phi \in [0, 90]^\circ$ to study how the distributions change over the cardiac cycle, where $\phi = 0^\circ$ is completely out-of-plane and $\phi = 90^\circ$ is completely in-plane.

3.4 Statistical analysis

Our complete strain rate tensor framework has the ability to assess 2D strain rate in a single slice LV model and 3D strain rate in a whole-LV model, and now we can apply it in a statistical analysis of our own design in an attempt to identify effects of regional myocardial dysfunction and how it develops over time. We will apply our Python framework to all datasets of rat hearts and collect characteristic curve parameters that represent myocardial function of the LV and see how these change over days after operation. We will divide Sham and MI hearts into respective groups, with Sham acting as control group, and compare them. Strain and strain rate measurements will be compared to other studies on LV dysfunction in rat hearts as a way to prove the viability of the numerical implementation of the Selskog method.

We plan to structure our statistical analysis in a way that lets us see if the infarcted hearts show trends over time that deviate from the control group, and could indicate the effects myocardial dysfunction. Based on previous studies, we expect to see reduction of strain and strain rate magnitudes locally in infarcted and adjacent tissue (31) (32) and globally over time as the infarct tissue grows (33). We also expect to see an increase

in dyssynchrony between segments in the MI group. This will be parameterised as Systolic Dyssynchrony Index (SDI); the standard deviation between the time points of the regional strain peaks as a percentage of the whole cardiac cycle duration to be able to compare measurements between rats with different heart rates (34). Higher values represent a higher level of dyssynchrony between the LV segments.

Strain rate angle distributions, as discussed previously in section 3.3.8, have never been produced before to assess myocardial dysfunction. This means that we cannot directly compare these results with previous studies, so for us to be able to interpret any systematic differences between the Sham and MI groups we need to see those results in the context of the whole picture.

The following sections go into details regarding all parameters that will be analysed and the specific methods of statistical analysis we plan to use.

3.4.1 Parameter overview

The parameters we will collect for the in-plane 2D strain rate tensor analysis, from all TPM datasets, are:

Condition - (1 = MI, 0 = Sham)

Time [days] - Time after operation

GRS [%] - Global Radial Strain peak

GCS [%] - Global Circumferential Strain peak

GRSRs [s^{-1}] - Systolic Global Radial Strain Rate peak

GRSRd [s^{-1}] - Diastolic Global Radial Strain Rate peak

GCSRs [s^{-1}] - Systolic Global Circumferential Strain Rate peak

GCSRd [s^{-1}] - Diastolic Global Circumferential Strain Rate peak

RSDI [%] - Radial Systolic Delay Index

CSDI [%] - Circumferential Systolic Delay Index

TSS [°] - Systolic Theta Stretch

TSd [°] - Diastolic Theta Stretch

TCs [°] - Systolic Theta Compression

TCd [°] - Diastolic Theta Compression

"Diastolic" strain rate peak is equivalent to what is commonly referred to as "early diastolic" strain rate peak in literature (35). The theta distribution parameter definitions

are original to this thesis, and were determined after studying angular distributions of Sham and MI hearts. We will discuss our choice of these parameters and their definitions in section 4.1.4 in relation to these plots.

For analysis using 3D strain rate tensors using the whole-LV segmentation model, additional parameters will be collected to describe motion out of the SHAX plane:

$GLS [\%]$ - Global Longitudinal Strain peak

$GLSRs [s^{-1}]$ - Systolic Global Longitudinal Strain Rate peak

$GLSRd [s^{-1}]$ - Diastolic Global Longitudinal Strain Rate peak

$PSs [^\circ]$ - Systolic Phi Stretch

$PSd [^\circ]$ - Diastolic Phi Stretch

$PCs [^\circ]$ - Systolic Phi Compression

$PCd [^\circ]$ - Diastolic Phi Compression

where "global" in this case refers to a weighted average sum of peak values across all LV slices used.

We will also look at the difference between angle distribution parameters measured in the basal and apical half of the LV, to investigate if heterogeneity in strain rate direction across slices can be linked to myocardial dysfunction. From visually studying angle distribution heterogeneity in the whole LV model, we determined to look at this specifically during systole. This choice will be discussed later in section 4.2.3 in relation to plots. These measurements will be denoted with a Δ ; ΔTSs and ΔTCs .

We will use the Pandas module in a Python script to organize all of the parameters measured during analysis for each dataset and save it as a "dataframe" structure, which lets us intuitively group measurements to suit our statistical models.

3.4.2 Linear regression

When plotting the measurements as a function of days after operation, and grouping them by Sham and MI, we will get scatter plot distributions that can reveal differences between the groups. We are interested in mean values for each group, but also to quantify how they change over time and whether or not this change is significant. For this we will use linear regression to estimate a regression line $y(t)$:

$$y(t) = t\beta_1 + \beta_0, \quad (3.7)$$

where β_0 is the y-axis intercept of the linear fit, β_1 is the slope value and t is time in days after operation. Using the "linregress()" function for least squares linear

regression from the `scipy.stats` module to calculate these values, we also get a p-value ($p \in [0, 1]$) that relates to β_1 . A lower value indicates that the linear fit model is more confident in the β_1 value and indicates that the change over time is systematic. By convention, we are going to assume that $p < 0.05$ disproves the null hypothesis (that any apparent change is random) and indicates statistical significance (cite?).

Despite our assumption of a linear change over time, the changes could be more complex in reality. However, we are limited by a small dataset. Because of this, we have decided that a simple linear regression model is appropriate and can still reveal interesting progression in our data. 95 percentile confidence intervals will be plotted along with the linear fits as a visual error estimate, representing an area that the regression model is confident that will contain 95% of regression lines from repeated measurements (cite?).

We will also calculate the 95% confidence interval specifically for the slope value from the standard error SE of the slope which we get as an output from `linregress()`. This estimate, assuming a normal distribution of possible slope values, can be calculated as $\pm 1.96 \cdot SE$ because the interval $(-1.96, 1.96)$ contains the inner 95% of the distribution (36).

3.4.3 T-tests

Another method we will use to assess whether the Sham and MI groups develop differently after operation is by performing T-tests at various points along the timeline. Unlike the linear regression, where we will use all measured data, we will now only look at the data from the first time point (day 1) and the last time point (day 40+) for each rat heart. "Day 40+" refers to the fact that there is some variation between the different rats in the timing of their last day of MR acquisition due to scheduling, from 40 to 45 days after operation. Mean values for both groups at these time points, with p-values calculated from independent two-sample T-tests (`ttest_ind()` from `scipy.stats`), will give us insight into whether the Sham and MI hearts developed differently from the start to the end of the study and if these differences are statistically significant.

We once again assume that $p < 0.05$ indicates statistical significance. However, when we make observations based on the statistical analysis we have designed we should keep in mind the possibility of reaching false conclusions, even with favorable p-values. A type-1 error ("false positive") refers to cases where statistical significance is declared where it is not actually true in the study population, and a type-2 error ("false negative") is when significance is rejected where it actually is true. The small sample size of our study makes it especially vulnerable to these errors (37).

We should also avoid discarding observations related to a p-value that does not meet the conventional significance condition without a second thought. Even if we determine that the difference between two mean values are not statistically significant, it does not mean that there is a significant similarity between them and there could still be interesting observations to make from such measurements despite the model not being as confident.

Chapter 4

Results

This chapter presents the results produced by our Python analysis framework. We have produced plots of strain rate, strain, and eigenvector angle distributions from the cardiac cycles of Sham and MI rat hearts. We have collected curve parameters that were used in statistical analysis to attempt to detect reduction in myocardial function and link it to MI progression.

We have separated the results into two sections, one regarding 2D strain rate tensor analysis of the basal-slice LV model, and one using 3D strain rate tensors on the whole-LV model. This gives us two stages of analysis complexity and two ways of looking at regional variation of the deformation parameters.

4.1 2D strain rate tensor analysis

Results in this section were acquired from analyzing in-plane motion in a single basal LV slice using 2D strain rate tensors.

4.1.1 Visualization

Figure 4.1 demonstrates the ellipse plot framework in action in two different time points, showing 2D strain rate tensors represented within the mask. The voxels are sampled in a grid with spacing of one voxel between each element for the sake of visibility. For quantitative results, however, we always utilize all of the voxels within the myocardium mask. The ellipse opacity corresponds to the invariant $I = \lambda_1^2 + \lambda_2^2$ from Equation 2.5 to give another visual reference for the strain rate magnitude in each tensor.

We have also used our ellipse plotting tool to visually evaluate the effectiveness of the velocity smoothing function (Equation 3.1) by looking for border artifacts in plots with tensors sampled in all masked voxels of a Sham heart. Equivalent example plots using an eroded mask, and one excluding tensors with only positive or negative eigenvalues, were also produced for the sake of comparison in Figure 4.2. In the figure, it is apparent

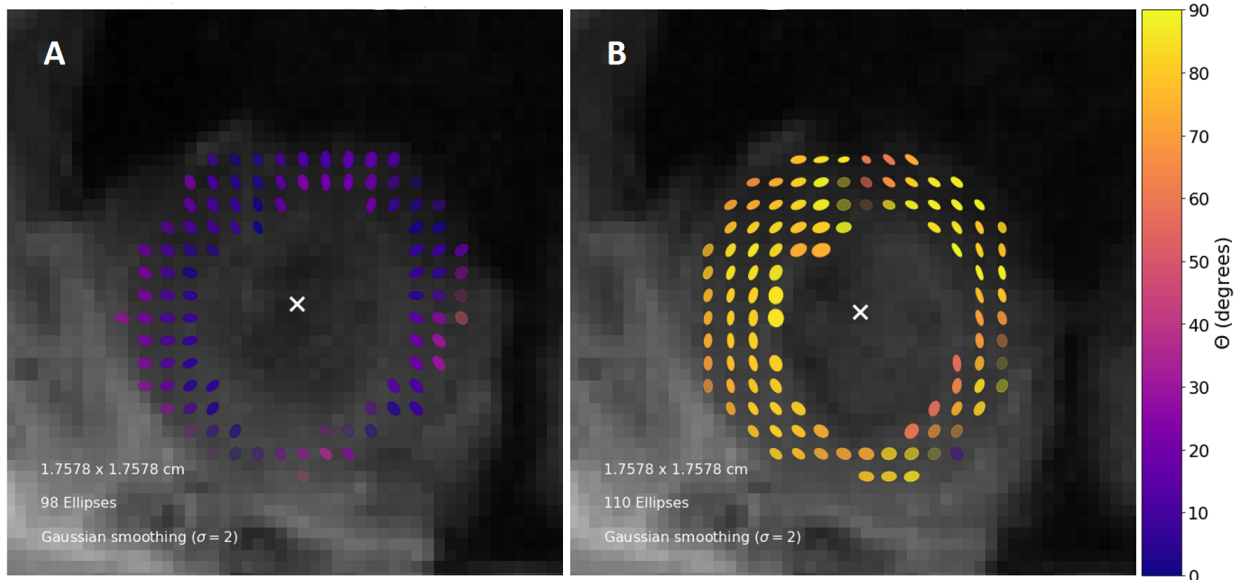


Figure 4.1: Ellipse plots of a Sham heart with color scale defined by the direction of most positive eigenvalue relative to the radial direction from the heart center (marked 'X'). A: Mid systole, with the myocardium experiencing stretching in the radial direction and compression in the circumferential direction. B: Early diastole, stretch along the circumferential direction and compression in the radial.

that exclusion removes ellipses at the mask borders at the endo- and epicardium that are abnormally small or large, which could be caused by border artifacts in the velocity gradient. Erosion appears to exclude some of these and more, while keeping some of the ellipses that were removed via exclusion. The eroded LV mask is noticeably thinner than its counterparts, having removed the inner and outer layer of voxels.

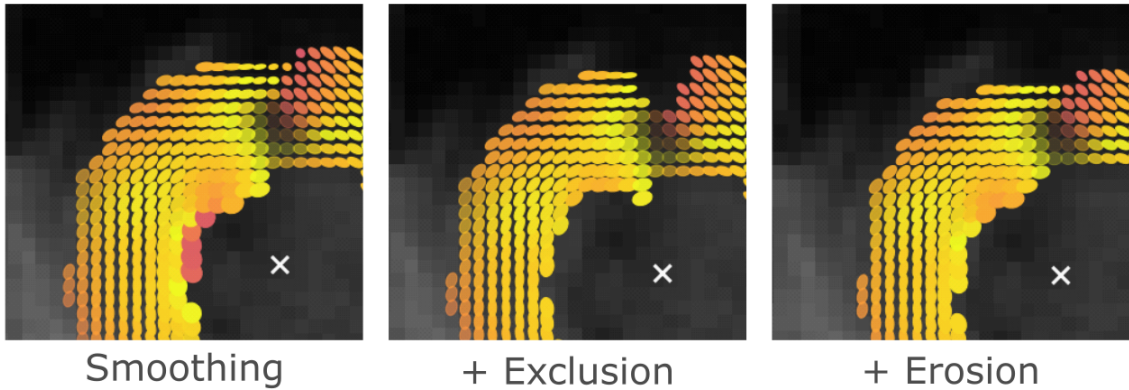


Figure 4.2: Details of strain rate tensor fields at the same time point as shown in Figure 4.1B, but sampling every voxel within mask. The leftmost tensor field was calculated from a velocity field smoothed by Equation 3.1, with no further correction. Effects of correction via exclusion and erosion, separately, in addition to smoothing are demonstrated as well.

4.1.2 Global strain rate and strain

Figure 4.3 demonstrates an example of measured radial and circumferential strain rate curves over one cardiac cycle, as well as their corresponding strain curves calculated using forward and backward integration over time as described in section 3.3.6. For

smoothing of the strain rate curve a kernel size of $N = 4$ was chosen for the running average function. Systolic and diastolic global strain rate peak measurements (as established in section 3.4.1) are marked, as well as peak global strain values.

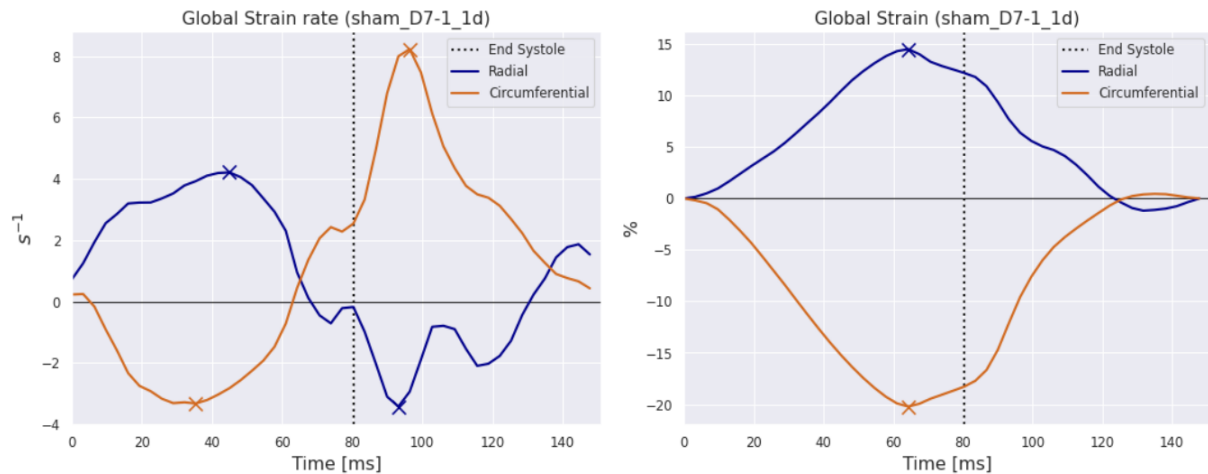


Figure 4.3: Global strain rate and strain curves from a single basal LV slice. Collected peak points are plotted as "X".

4.1.3 Regional strain rate and strain

Figure 4.4 shows examples of ellipse and strain plots for a Sham and MI heart where the LV has been divided into groups to look at regional variation. Peak values on the strain curves that are collected for later statistical analysis are marked. Ellipse opacity is still modulated by strain rate magnitude, and reveals lower values in the infarct tissue in the red group.

4.1.4 Eigenvector angle distribution

Figure 4.5 shows examples of how the θ angle distributions for a Sham and a late stage MI heart can look like, grouped based on whether they describe the direction of stretch or compression, change over the cardiac cycle. To the extent of our knowledge, this kind of plot has never been used to analyze LV motion before. We will therefore take a moment to describe it extensively here.

The angle data are plotted over time, where we see that the scatter points describing direction of stretch and compression concentrate in opposite ends of the y-axis in systole and swap sides in diastole. During systole, compression angles concentrate toward $\theta = 90^\circ$ and stretch concentrates toward $\theta = 0^\circ$ relative to the radial axis. In other words, more compression happens in the circumferential direction and more stretching is happening in the radial direction during systole. The opposite can be seen during diastole.

The curves with colors corresponding to the distributions represent the mean angle at every time point, and appear cyclic with distinct peaks and minima. It also appears

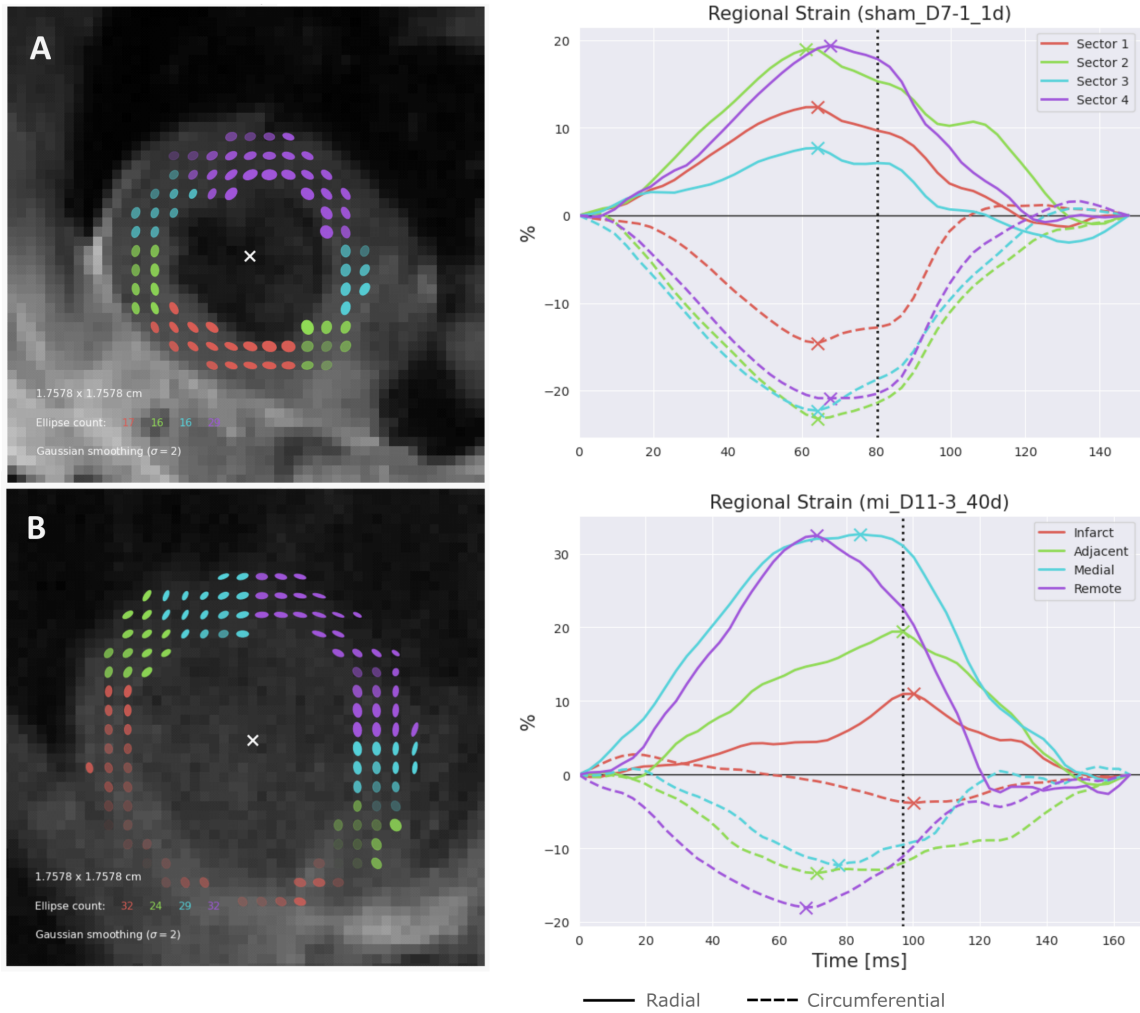


Figure 4.4: Regional strain analysis of a Sham and MI heart, featuring strain rate tensor ellipse plots at early diastole and strain plots with color coding based on group. The end systole time point is marked with a dotted line. A: Sham heart with arbitrary, numerated sectors. B: MI heart 40 days after infarction, groups based on infarct sector and proximity.

as if these curves are almost mirrored around $\theta = 45^\circ$, an angle that points equally in the radial and circumferential direction. This is a consequence of every 2D tensor having two orthogonal eigenvectors in the SHAX plane, where most of them contain one vector describing stretch and one describing compression.

The red and green distributions of the MI heart do not appear to be as distinct as in the Sham plot, where we see areas of white between them. Distributions like this appear to have curve peaks closer to $\theta = 45^\circ$ as they are less concentrated in the top and bottom of the y-axis and appear to 'bleed' more into each other.

Based on these visual observations of the angle distributions, we chose to attempt to use the peaks marked in Figure 4.5 as functional parameters where the peak values represent myocardial function. We speculate values closer to 45° , more heterogeneous distributions, to represent myocardial dysfunction. These are named as shown in the figure and their abbreviations are listed in section 3.4.

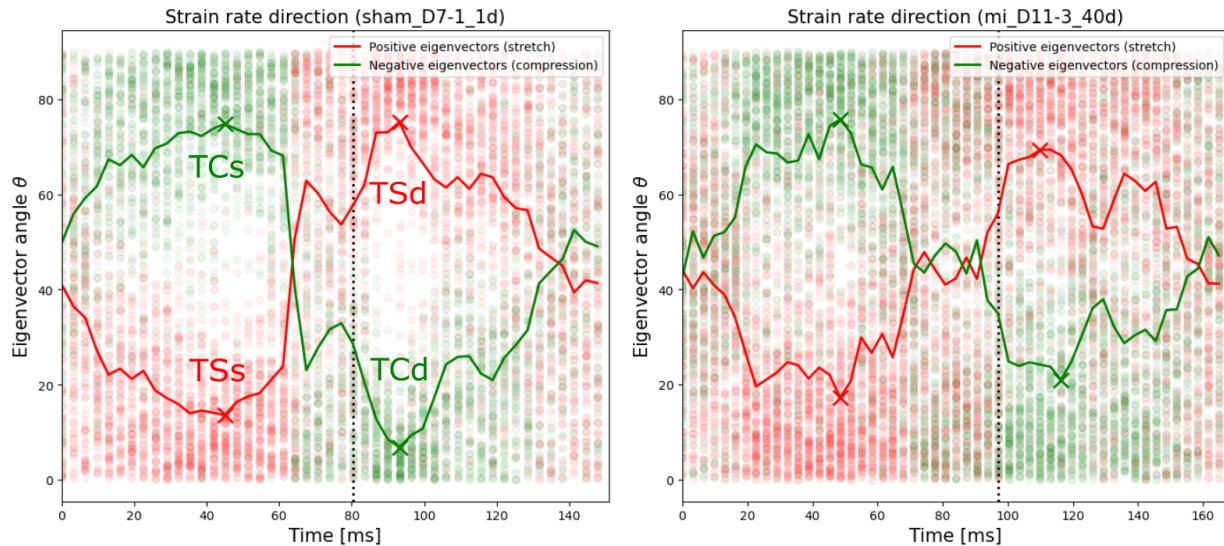


Figure 4.5: Distributions of tensor angles grouped by stretch (red) and compression (green) for a Sham (left) and MI (right) heart. Average angle for each time point represented by curves of corresponding color. Curve peaks and minima in systole and diastole are marked ("X").

This was only an initial attempt to visually recognize patterns in the distributions, and how they may be affected by MI. The results of our statistical analysis will be a foundation for deeper physiological interpretation.

4.1.5 MI progression

In this section we will show the results of the larger scale statistical analysis that we designed to describe how the different parameters progress over time in the Sham and MI groups.

Figure 4.6 shows the linear regression analysis for a selection of parameters that had low p-values ($p < 0.05$ and in one case slightly above 0.05) indicating confident slope values and significant change over time in days.

Figure 4.7 visualizes the T-test analysis for a selection of parameters at the first and last day after operation using barplots. A common thread with these plots is that they all initially ("day 1") show measurements that are not significantly different ($p > 0.05$) but gradually become significantly different ($p < 0.05$) over time. The implications of this will be discussed later.

The information presented in these plots are also summarized for all parameters established in section 3.4.1 in two tables. Table 4.1 shows a summary of all slope values from linear regression of the measurements of both groups with p-values corresponding to slope value. The confidence interval each slope is included as an error estimate. Table 4.2 shows mean values at the first and last time point (day 1 and "day 40+") of all hearts with standard deviation as error estimate. p-values calculated from independent two-sample T-tests indicate whether the Sham and MI groups are significantly different

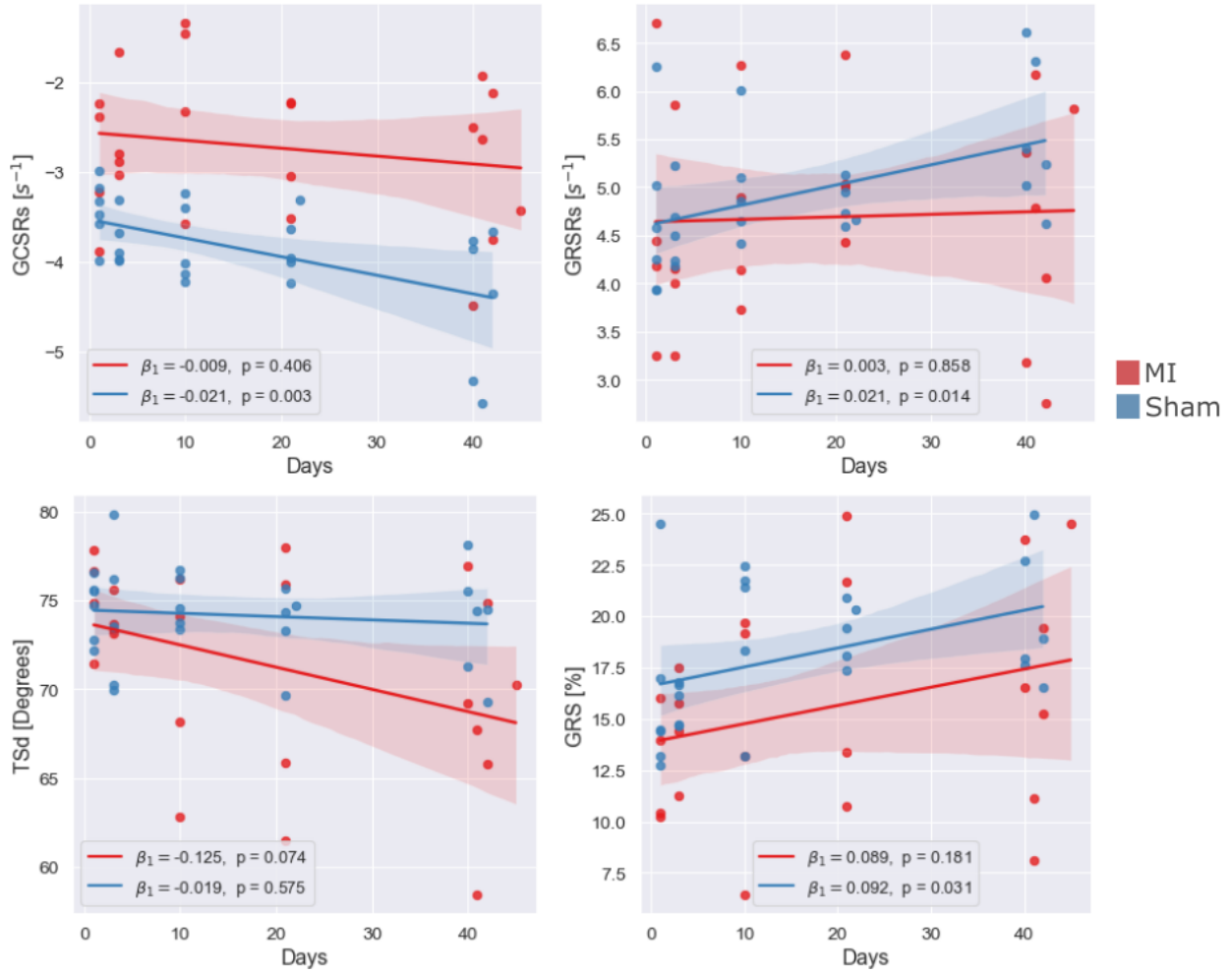


Figure 4.6: Scatter plots of a selection of measured parameters as a function of days and grouped by Sham (blue) and MI (red). Slope values β_1 from linear regression and corresponding p -values in legend, with 95% confidence intervals in the plot.

at the relevant time point.

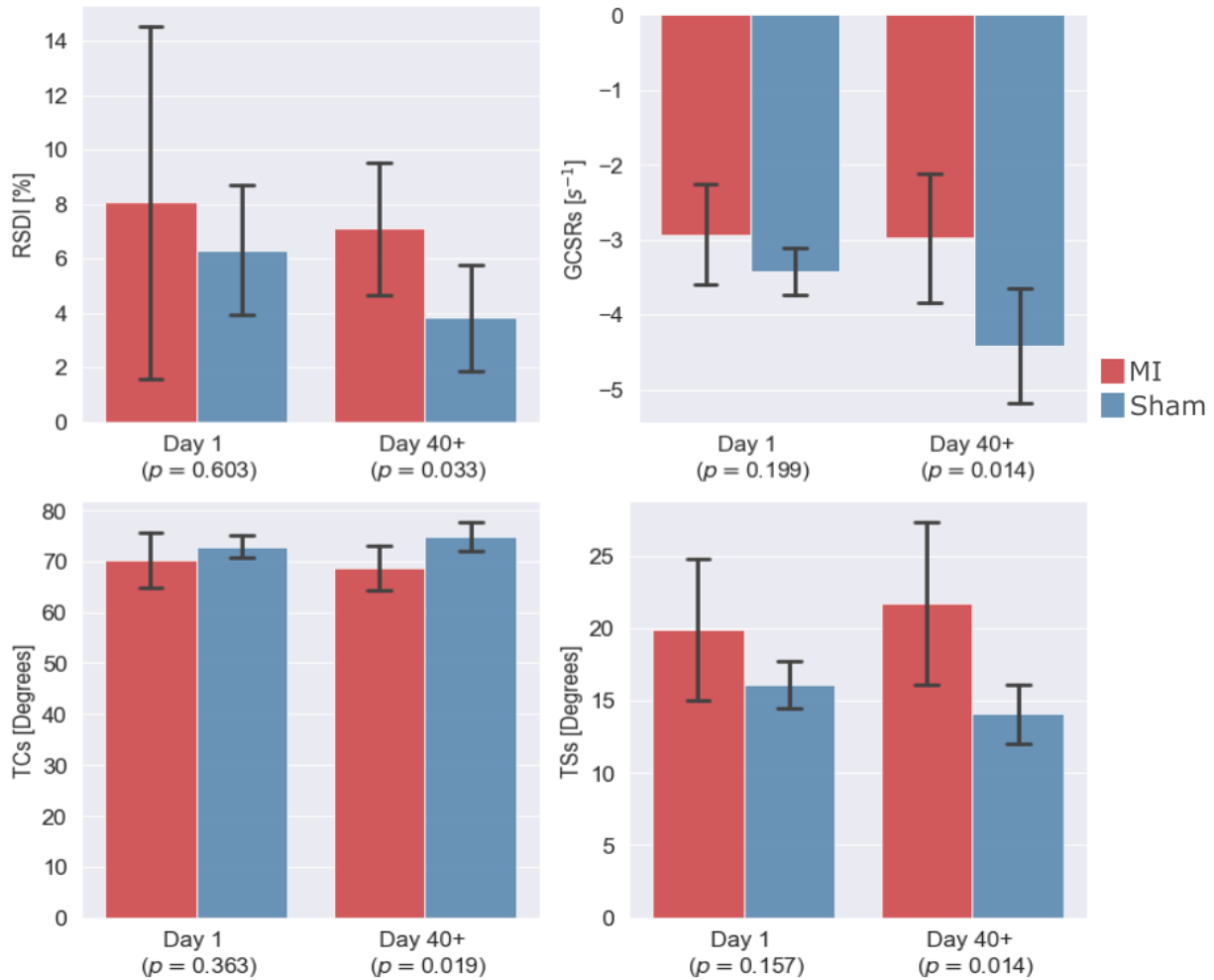


Figure 4.7: Barplots for a selection of parameters displaying mean values (with standard deviation error bars) of the MI and Sham groups at the first and last day after operation. p-values from independent two-sample T-tests.

	Sham		MI	
	β_1	p	β_1	p
GRS [%]	0.092 ± 0.079	.031	0.089 ± 0.126	.181
GCS [%]	-0.033 ± 0.055	.255	-0.010 ± 0.094	.835
GRSRs [s^{-1}]	0.021 ± 0.016	.014	0.003 ± 0.029	.858
GRSRd [s^{-1}]	-0.013 ± 0.033	.453	0.014 ± 0.052	.597
GCSR _s [s^{-1}]	-0.021 ± 0.012	.003	-0.009 ± 0.020	.406
GCSR _d [s^{-1}]	-0.017 ± 0.027	.230	-0.029 ± 0.038	.145
RSDI [%]	-0.051 ± 0.061	.118	-0.041 ± 0.127	.534
CSDI [%]	0.005 ± 0.053	.845	0.041 ± 0.097	.412
TSs [°]	-0.045 ± 0.051	.093	-0.001 ± 0.151	.988
TSd [°]	-0.019 ± 0.065	.575	-0.125 ± 0.131	.074
TCs [°]	0.031 ± 0.061	.322	-0.007 ± 0.138	.924
TCd [°]	0.055 ± 0.055	.062	0.131 ± 0.126	.054

Table 4.1: Slope values (β_1) from linear regression of Sham ($n = 27$) and MI ($n = 23$) data, with 95% confidence interval as error estimate ($\beta_1 \pm ci$). p-values correspond to slope estimate from linregression function.

	Day 1			Day 40+		
	Sham	MI	p	Sham	MI	p
<i>GRS</i> [%]	16.06 ± 4.38	12.67 ± 2.83	.211	19.79 ± 3.30	16.95 ± 6.13	.333
<i>GCS</i> [%]	-18.44 ± 2.18	-13.06 ± 1.91	.004	-19.82 ± 3.03	-13.58 ± 3.89	.009
<i>GRSRs</i> [s^{-1}]	4.66 ± 0.88	4.64 ± 1.47	.979	5.54 ± 0.77	4.59 ± 1.31	.150
<i>GRSRd</i> [s^{-1}]	-5.44 ± 0.80	-7.98 ± 1.48	.007	-6.33 ± 1.42	-7.01 ± 2.46	.565
<i>GCSR</i> s [s^{-1}]	-3.42 ± 0.35	-2.93 ± 0.77	.199	-4.42 ± 0.83	-2.98 ± 0.93	.014
<i>GCSR</i> d [s^{-1}]	7.73 ± 1.32	6.50 ± 0.43	.117	6.47 ± 1.00	5.05 ± 1.61	.089
<i>RSDI</i> [%]	6.30 ± 2.62	8.05 ± 7.47	.603	3.81 ± 2.15	7.09 ± 2.61	.033
<i>CSDI</i> [%]	1.63 ± 0.99	5.07 ± 1.48	.002	2.83 ± 3.30	7.01 ± 3.31	.044
<i>TSs</i> [°]	16.10 ± 1.77	19.88 ± 5.67	.157	14.07 ± 2.24	21.72 ± 6.04	.014
<i>TSd</i> [°]	74.57 ± 1.73	75.21 ± 2.80	.666	73.85 ± 3.15	69.03 ± 6.09	.110
<i>TCs</i> [°]	72.86 ± 2.32	70.23 ± 6.21	.363	74.80 ± 3.08	68.59 ± 4.72	.019
<i>TCd</i> [°]	10.18 ± 2.68	13.63 ± 3.02	.093	13.38 ± 2.49	19.75 ± 6.39	.043

Table 4.2: Mean measurements (mean ± std) at the first and last day after operation for Sham ($n = 12$) and MI ($n = 11$). P-values are based on two sample t-tests between the two groups.

4.2 3D strain rate tensor analysis

The results in this section were acquired from analyzing 3D motion in the whole LV segmentation model (see Figure 3.1 for a reminder) using 3D strain rate tensors. Global measurements for all slices, as well as regional measurements of the base and apical sections were used to study regional variation across or two defined halves of the LV.

4.2.1 Global strain rate and strain

(global curves, or straight to the stacked 2d plots?)

4.2.2 Regional strain rate and strain

4.2.3 Eigenvector angle distribution

4.2.4 (Progression / statistical analysis)

	Sham		MI	
	β_1	p	β_1	p
GRS [%]	0.102 ± 0.067	.008	0.05 ± 0.097	.325
GCS [%]	-0.084 ± 0.066	.023	-0.027 ± 0.116	.651
GLS [%]	-0.028 ± 0.047	.264	-0.039 ± 0.063	.234
GRSRs [s^{-1}]	0.019 ± 0.018	.048	0.009 ± 0.017	.298
GRSRd [s^{-1}]	-0.023 ± 0.015	.010	-0.013 ± 0.031	.404
GCSR _s [s^{-1}]	-0.021 ± 0.014	.010	-0.018 ± 0.024	.173
GCSRd [s^{-1}]	0.008 ± 0.024	.544	-0.012 ± 0.032	.460
GLSR _s [s^{-1}]	-0.006 ± 0.012	.361	-0.012 ± 0.013	.095
GLSRd [s^{-1}]	0.003 ± 0.014	.721	0.003 ± 0.014	.721
TS _s [°]	-0.033 ± 0.056	.263	-0.029 ± 0.099	.570
TS _d [°]	0.011 ± 0.051	.672	0.005 ± 0.088	.915
TC _s [°]	0.037 ± 0.043	.104	0.019 ± 0.066	.580
TC _d [°]	0.002 ± 0.066	.959	0.016 ± 0.095	.749
Δ TS _s [°]	-0.065 ± 0.065	.062	-0.027 ± 0.074	.489
Δ TC _s [°]	-0.041 ± 0.057	.175	-0.028 ± 0.068	.433
PS _s [°]	$xx \pm xx$.xx	$xx \pm xx$.xx
PS _d [°]	$xx \pm xx$.xx	$xx \pm xx$.xx
PC _s [°]	$xx \pm xx$.xx	$xx \pm xx$.xx
PC _d [°]	$xx \pm xx$.xx	$xx \pm xx$.xx

Table 4.3: Slope values (β_1) from linear regression of 3D Sham ($n = 21$) and MI ($n = 20$) data, with 95% confidence interval as error estimate ($\beta_1 \pm ci$). p-values correspond to slope estimate from linregression function.

	Day 1			Day 40+		
	Sham	MI	p	Sham	MI	p
<i>GRS</i> [%]	9.50 ± 1.52	7.59 ± 3.03	.303	13.57 ± 2.07	9.59 ± 4.26	.106
<i>GCS</i> [%]	-16.27 ± 2.25	-12.63 ± 3.39	.123	-19.50 ± 1.18	-13.35 ± 3.47	.007
<i>GLS</i> [%]	-5.05 ± 1.06	-4.13 ± 1.88	.429	-6.82 ± 1.49	-5.80 ± 1.36	.322
<i>GRSRs</i> [s^{-1}]	3.28 ± 0.57	2.26 ± 0.51	.037	3.91 ± 0.52	2.69 ± 0.61	.014
<i>GRSRd</i> [s^{-1}]	-1.85 ± 0.50	-2.70 ± 0.94	.162	-2.90 ± 0.25	-2.97 ± 1.89	.936
<i>GCSR</i> [s^{-1}]	-3.21 ± 0.15	-2.51 ± 0.84	.149	-4.08 ± 0.44	-3.11 ± 0.93	.078
<i>GCSRd</i> [s^{-1}]	5.30 ± 1.19	4.88 ± 0.79	.578	5.25 ± 0.29	3.89 ± 0.90	.014
<i>GLSRs</i> [s^{-1}]	-1.30 ± 0.28	-0.97 ± 0.24	.126	-1.58 ± 0.39	-1.46 ± 0.47	.671
<i>GLSRd</i> [s^{-1}]	1.80 ± 0.30	1.67 ± 0.40	.622	1.93 ± 0.53	1.59 ± 0.25	.291
<i>TSs</i> [°]	30.39 ± 0.62	33.67 ± 3.65	.127	28.93 ± 1.23	32.70 ± 4.82	.131
<i>TSd</i> [°]	57.53 ± 1.71	57.80 ± 2.65	.871	57.96 ± 1.52	57.30 ± 5.35	.798
<i>TCs</i> [°]	58.93 ± 1.34	56.21 ± 2.40	.095	60.19 ± 1.30	57.02 ± 3.33	.088
<i>TCd</i> [°]	29.46 ± 2.67	31.14 ± 2.87	.423	29.94 ± 1.75	32.71 ± 4.89	.272
ΔTSs [°]	1.96 ± 2.03	3.96 ± 2.53	.236	0.55 ± 0.61	3.23 ± 1.92	.020
ΔTCs [°]	1.58 ± 1.85	3.17 ± 2.81	.381	1.08 ± 0.36	2.57 ± 1.09	.023
<i>PSs</i> [°]	$xx \pm xx$	$xx \pm xx$.xx	$xx \pm xx$	$xx \pm xx$.xx
<i>PSd</i> [°]	$xx \pm xx$	$xx \pm xx$.xx	$xx \pm xx$	$xx \pm xx$.xx
<i>PCs</i> [°]	$xx \pm xx$	$xx \pm xx$.xx	$xx \pm xx$	$xx \pm xx$.xx
<i>PCd</i> [°]	$xx \pm xx$	$xx \pm xx$.xx	$xx \pm xx$	$xx \pm xx$.xx

Table 4.4: Mean measurements (mean \pm std) at the first and last day after operation for 3D Sham ($n = 9$) and MI ($n = 8$) data. P-values are based on two sample t-tests between the two groups.

Chapter 5

Discussion

The aim of this thesis was to demonstrate that the Selskog method, involving strain rate tensors from PC-MRI velocity data, are a viable tool to analyze regional LV dysfunction after infarct as well as investigating the implemented framework's further potential for new kinds of analysis. We have, for the first time, described myocardial dysfunction using heterogeneity of strain rate direction and we will attempt to relate these measurements to the more established parameters. In this chapter, we will discuss our results and their physiological implications in detail and compare observations and measurements to similar studies.

5.1 2D strain rate tensor analysis

5.1.1 Tensor Visualization

As seen in Figure 4.1 our framework produces ellipse plots that visualize strain rate tensors in the LV comparable to literature when it comes to their shape and orientation at various time points (29). During systole, the plot shows expansion in the radial direction and compression in the circumferential. In the diastole frame we see the opposite. The plots also map ellipse color based on the direction of stretch, or the most positive eigenvalue. Even though the direction of strain rate appears relatively homogenous across the myocardium at these frames, we can also see some variation in hue. The distribution of strain rate directions will be discussed later.

In Figure 4.4 we display an alternative color scheme that distinguishes between the different LV groups used for regional analysis. Here, we also see clearly the reduced total strain rate in the MI heart infarction sector from the reduced ellipse opacity. The highest strain rate values appear to be in the medial and remote group in the MI heart which is visualized by ellipses that appear more "squeezed". This is supported by the corresponding strain curve peaks for the different sectors.

We used ellipse plots to visually assess the effectiveness of the velocity smoothing. Figure 4.2 illustrates the observed differences between the suggested methods. Exclusion appears to remove ellipses affected by border artifacts with precision. Erosion appears

to remove the most intense artifacts while having a possibility of keeping some of them, depending on the quality of the LV mask, in addition of having a more consistent LV shape with no random sections missing.

In the end we decided to go for the simplest alternative and just apply smoothing, with no additional correction. This lets us keep more voxels of data, and we don't risk excluding tensors that may describe complex motion out of plane that appear as if conservation of mass is broken. This choice was also made with trust in the theory established by Selskog et al., in the segmented LV masks designed for the TPM data and the black blood MR sequence used to suppress noisy blood data during acquisition. As a last measure of comparison, we performed the entire statistical analysis using all three alternatives and all results were quite similar (mean-, slope- and p-values). This implies that the corrections don't make a useful difference, and that we might as well choose a simpler operation.

Our strain rate tensor visualization framework appears to produce tensor fields and ellipse plots as we intended, with tensor color palettes and opacity visually communicating regional variation in strain rate.

5.1.2 Global strain rate and strain

Figure 4.3 shows an example of a strain rate curve and a corresponding integrated strain curve for a Sham heart. From the strain rate plot we see radial expansion and circumferential contraction during systole and the opposite during diastole. Integrating gives a positive peak for the radial strain curve and a negative peak for the circumferential, indicating that the LV circumference contracts and that the LV wall thickness expands as the LV contracts. The radial strain curve also clearly displays a later diastolic peak, which has not been marked. Despite being used in clinical studies (38), our plots do not show the late diastolic strain rate peaks consistently and so we have chosen to focus only on systolic and early diastolic strain rate peaks.

Table 4.1 contains the results of the linear regression analysis, where we observe that systolic strain rate magnitudes in the Sham group increases significantly over time (GRSRs and GCSRs slopes have p-values .014 and .003). This could be due to the fact that the rats were young during the TPM acquisitions, and that the healthy hearts were still developing and changing. The MI hearts do not see such a systematic change over time, and their hearts may be struggling to keep up with the development of their healthy counterparts. This aging effect is important to keep in mind in later discussion when we use the Sham group as a control group.

We see in Table 4.2 that the mean measurements of GCS, GCSRs and GCSRd in the Sham control group are comparable to literature applying PC-CMR techniques and speckle tracking to the same rat MI-model that our analysis gets its data from (24)(31). "PC-CMR techniques" in this case refers to calculating strain via displacement, as discussed in section 2.3. These studies also observed lower GCS in the MI hearts than in Sham, which is replicated in our results. In addition, we observe that GCS appears to show an immediate reduction in function in the MI group, with no significant change

over time (p-values .004 and .009 at first and last day respectively). (more to say on this?)

Lower GRS is observed in the MI group compared to Sham, which we expected based on literature studying LV deformation in rat hearts (39). However, the mean magnitude of this parameter (19.79% in Sham at 40+ days) is not comparable as it is significantly lower, where GRS in literature has been found to have values around 25% and 40% in healthy myocardium in rats of similar weight and age to the rats in our MI model. (comparable systolic strain rate c and r, very low diastolic radial strain rate compared to circ)

(radial strain peaks not comparable to literature? consequence of tensor calculation? what else is different in our study?) (relevant to the circumferential orientation of myocytes?) (poor GRS due to cylindrical LV model?)

(systolic strain rate curve linreg slopes have lowest p-values, most decisive change via aging. aging affects systole the most?)

5.1.3 Regional strain rate and strain

We can visually assess regional variation from the ellipse plots discussed previously, and quantitatively using strain curves grouped by sector. Figure 4.4A shows an ellipse plot of a Sham LV at early diastole, where we observe a relatively consistent ellipse opacity indicating a homogeneous distribution of strain rate magnitude during LV relaxation. The corresponding strain curves, especially for circumferential strain show similar peak values that appear to occur pretty much simultaneously which supports the visual observation. The radial strain curves appear to show more variation.

Figure 4.4B shows a similar ellipse and regional strain plot for an MI LV 40 days after infarct. Compared to the Sham heart, this ellipse plot clearly shows local dysfunction in the infarct tissue visually from the dimmed ellipse color and from the lower strain peaks in the infarct compared to the other sectors. We can also observe visually from the ellipse plot that the remote sector in the MI LV contains thinner and longer tensors than we see elsewhere which also indicates higher strain rate magnitude. This could be an effect of remodeling, where the tissue further from the infarct compensates for the loss of function. These observations are also comparable to literature (31).

Comparing the circumferential peaks in Figure 4.4 it appears that the dyssynchrony in peak time between sectors is larger in the MI heart. Looking into this in our statistical analysis, we see in Table 4.2 that CSDI and RSDI mean values are lower in the Sham group. We also see that T-tests comparing RSDI with the MI group scores $p > 0.05$ initially and $p < 0.05$ at the last time point, implying that the dyssynchrony of the MI LV gradually increases and significantly deviates from the control group as the infarct grows. These observations are supported by literature, where it has been shown that circumferential SDI estimates are lower and have less variance in healthy control groups compared to hearts inflicted by cardiac disease (40). Physiologically, this delay could be caused by the fact that more infarct tissue is being pulled by its functional neighboring muscle tissue instead of actively deforming itself on time.

5.1.4 Eigenvector angle distribution

The first observation we made from the distributions in Figure 4.5 is that the average angle of stretch and compression over time seem to compliment the strain rate curves. Just like the strain rate curves, the average angles tell us that stretching happens more in the radial direction during systole and more in the circumferential direction in diastole, opposite for compression.

The angle distributions, however, make it clear that there is a range of directions even in the Sham hearts when the angle concentration is highest. This implies that the LV shortening and wall thickening do not happen completely in the radial and circumferential directions assumed by conventional LV geometry. We technically already observed and noted this when discussing the ellipse plots in Figure 4.1, where this heterogeneity can be seen from the ellipse color scale based on the same θ range as the angle distributions.

We attempted to quantify angle heterogeneity from the peak values, and we see that the MI example plot in the figure has peaks closer to 45° and a more heterogeneous distribution. From Table 4.2 we observe that this is the case for all mean measurements of the TSs, TSd, TCs and TCd peak values of late stage MI compared with Sham. From the same table we also observe that the difference between TSs, TCs and TCd measurements in Sham and MI groups is not initially statistically significant but becomes significant ($p < 0.05$) in the late stage. This implies that these parameters are affected by MI and that the distributions in the MI group become gradually more heterogeneous as the infarct tissue grows.

Assuming that increased angle distribution heterogeneity is an indicator of myocardial dysfunction, what is the physiological and mechanical interpretation of this? Our speculation is that this gives insight into the coordination of the myocardium, and relates to how responsive it is to electrical signals. It has been shown before that dyssynchrony can be related to myocardial dysfunction (11), and this was also observed in our own analysis via the CSDI and RSDI parameters. This could relate to our angle distributions, where dyssynchrony between different sections of the LV could cause it to respond at different times and makes the distributions less focused if the different sectors are at their most homogenic at different times. We also suspect that the strain rate tensors in the infarct tissue to have a wider range of angles, as they describe low magnitude deformation as a result of being pulled by healthier muscle tissue which is a less controlled movement than active, higher magnitude deformation.

These findings also put our strain rate measurements in a new light. The components of the vector decomposition used to measure strain rate were the eigenvalue and eigenvector of the strain rate tensor, representing the magnitude and *direction* of strain rate. We have now shown that the eigenvector angles themselves can be related to myocardial function, which illustrates that not only the magnitude of deformation but also the coordination of the myocardium on voxel scale are important factors in strain analysis. In addition, the fact that the mean curves in Figure 4.5 are roughly symmetric confirms that most 2D strain rate tensors in the LV describes stretch in one direction and compression in an orthogonal direction. The way we define $\theta \in [0, 90]^\circ$ means that any

angle $\theta_2 = \theta_1 + 90^\circ$ in the range will be mirrored around 45° .

(2d summary, circ SDI and T parameters, proof of concept)

5.2 3D strain rate tensor analysis

(phi uninterpretable, transmural variation?)

5.3 Limitations and future research (move to conclusion?)

We have demonstrated the potential of strain rate tensor analysis and its ability to visually and quantitatively assess regional myocardial dysfunction in two and three spatial dimensions. However, there are limitations to our framework and further potential in the application of strain rate tensors.

(GRS, GLS) (more advanced segmentation models, 3d c.o.m., nice 3d visualization/animation) (complications with GLS using SHAX slices?)

(transmural variation, relate to phi and Bårds work)

(combine 2d and 3d analysis, are 2d tensor theta distributions a stronger tool?)

(rat model, study population size)

Chapter 6

Conclusion

(diagnostic value of findings?)

Bibliography

- [1] G. Savarese, P. M. Becher, L. H. Lund, P. Seferovic, G. M. C. Rosano, and A. J. S. Coats. Global burden of heart failure: a comprehensive and updated review of epidemiology. *Cardiovasc Res*, 118(17):3272–3287, 2023. 1
- [2] G. Savarese and L. H. Lund. Global public health burden of heart failure. *Card Fail Rev*, 3(1):7–11, 2017. 1
- [3] S. Heo, T. A. Lennie, C. Okoli, and D. K. Moser. Quality of life in patients with heart failure: ask the patients. *Heart Lung*, 38(2):100–8, 2009. 1
- [4] NIH NHLBI. What is heart failure? 2022. <https://www.nhlbi.nih.gov/health/heart-failure>, accessed 26.02.24. 1
- [5] Cleveland Clinic. Heart attack: symptoms, causes treatment. 2024. <https://my.clevelandclinic.org/health/diseases/16818-heart-attack-myocardial-infarction>, accessed 04.04.24. 1, 2.2.2
- [6] R. Folse and E. Braunwald. Determination of fraction of left ventricular volume ejected per beat and of ventricular end-diastolic and residual volumes. experimental and clinical observations with a precordial dilution technic. *Circulation*, 25:674–85, 1962. 1
- [7] A. Scatteia, A. Baritussio, and C. Bucciarelli-Ducci. Strain imaging using cardiac magnetic resonance. *Heart Fail Rev*, 22(4):465–476, 2017. 1
- [8] E. K. Espe. Measuring in vivo regional myocardial function using high field mri. 2014. University of Oslo, Oslo. 1, 2.3, 2.3
- [9] F. Valente, L. Gutierrez, L. Rodriguez-Eyras, R. Fernandez, M. Montano, A. Sao-Aviles, V. Pineda, A. Guala, H. Cuellar, A. Evangelista, and J. Rodriguez-Palomares. Cardiac magnetic resonance longitudinal strain analysis in acute st-segment elevation myocardial infarction: A comparison with speckle-tracking echocardiography. *Int J Cardiol Heart Vasc*, 29:100560, 2020. 1
- [10] J. J. Hjertaas, E. Einarsen, E. Gerdts, M. Kokorina, C. A. Moen, S. Urheim, S. Saeed, and K. Matre. Impact of aortic valve stenosis on myocardial deformation in different left ventricular levels: A three-dimensional speckle tracking echocardiography study. *Echocardiography*, 40(10):1028–1039, 2023. 1, 3.2

- [11] P. Lim, A. Buakhamsri, Z. B. Popovic, N. L. Greenberg, D. Patel, J. D. Thomas, and R. A. Grimm. Longitudinal strain delay index by speckle tracking imaging: a new marker of response to cardiac resynchronization therapy. *Circulation*, 118(11):1130–7, 2008. 1, 5.1.4
- [12] M. J. Gotte, T. Germans, I. K. Russel, J. J. Zwanenburg, J. T. Marcus, A. C. van Rossum, and D. J. van Veldhuisen. Myocardial strain and torsion quantified by cardiovascular magnetic resonance tissue tagging: studies in normal and impaired left ventricular function. *J Am Coll Cardiol*, 48(10):2002–11, 2006. 1
- [13] G. Pedrizzetti, P. Claus, P. J. Kilner, and E. Nagel. Principles of cardiovascular magnetic resonance feature tracking and echocardiographic speckle tracking for informed clinical use. *J Cardiovasc Magn Reson*, 18(1):51, 2016. 1
- [14] O. A. Smiseth, H. Torp, A. Opdahl, K. H. Haugaa, and S. Urheim. Myocardial strain imaging: how useful is it in clinical decision making? *Eur Heart J*, 37(15):1196–207, 2016. 1
- [15] P. Selskog, E. Heiberg, T. Ebbers, L. Wigström, and M. Karlsson. Kinematics of the heart: strain-rate imaging from time-resolved three-dimensional phase contrast mri. *IEEE Trans Med Imaging*, 21(9):1105–9, 2002. 1, 2.3, 3.3.1, 3.3.2, 3.3.3
- [16] A. Bjørnerud and E. K. Espe. *Physics of MR imaging: Compendium for FYS4740/9740*. 2023. 2.1
- [17] Cleveland Clinic. What is the heart? 2024. <https://my.clevelandclinic.org/health/body/21704-heart>, accessed 07.03.24. 2.2.1
- [18] Cleveland Clinic. What is the pulmonary valve? 2024. <https://my.clevelandclinic.org/health/body/24273-pulmonary-valve>, accessed 05.04.24. 2.2.1
- [19] H. Fukuta and W. C. Little. The cardiac cycle and the physiologic basis of left ventricular contraction, ejection, relaxation, and filling. *Heart Fail Clin*, 4(1):1–11, 2008. 2.2.1
- [20] Radiopaedia. Late gadolinium enhancement. 2023. <https://radiopaedia.org/articles/late-gadolinium-enhancement-2>, accessed 04.04.24. 2.2.2
- [21] D. Westermann, M. Kasner, P. Steendijk, F. Spillmann, A. Riad, K. Weitmann, W. Hoffmann, W. Poller, M. Pauschinger, H. P. Schultheiss, and C. Tschope. Role of left ventricular stiffness in heart failure with normal ejection fraction. *Circulation*, 117(16):2051–60, 2008. 2.2.2
- [22] S. Frantz, M. J. Hundertmark, J. Schulz-Menger, F. M. Bengel, and J. Bauersachs. Left ventricular remodelling post-myocardial infarction: pathophysiology, imaging, and novel therapies. *Eur Heart J*, 43(27):2549–2561, 2022. 2.2.2
- [23] J. M. Wakeling, S. A. Ross, D. S. Ryan, B. Bolsterlee, R. Konno, S. Dominguez, and N. Nigam. The energy of muscle contraction. i. tissue force and deformation during fixed-end contractions. *Front Physiol*, 11:813, 2020. 2.3

- [24] E. K. S. Espe, J. M. Aronsen, M. Eriksen, O. M. Sejersted, L. Zhang, and I. Sjaastad. Regional dysfunction after myocardial infarction in rats. *Circ Cardiovasc Imaging*, 10(9), 2017. 3.1, 5.1.2
- [25] E. K. Espe, J. M. Aronsen, B. Skrbic, V. M. Skulberg, J. E. Schneider, O. M. Sejersted, L. Zhang, and I. Sjaastad. Improved mr phase-contrast velocimetry using a novel nine-point balanced motion-encoding scheme with increased robustness to eddy current effects. *Magn Reson Med*, 69(1):48–61, 2013. 3.1.2
- [26] E. K. Espe, J. M. Aronsen, K. Skardal, J. E. Schneider, L. Zhang, and I. Sjaastad. Novel insight into the detailed myocardial motion and deformation of the rodent heart using high-resolution phase contrast cardiovascular magnetic resonance. *J Cardiovasc Magn Reson*, 15(1):82, 2013. 3.1.2
- [27] W. Kroon, T. Delhaas, P. Bovendeerd, and T. Arts. Structure and torsion in the normal and situs inversus totalis cardiac left ventricle. ii. modeling cardiac adaptation to mechanical load. *Am J Physiol Heart Circ Physiol*, 295(1):H202–10, 2008. 3.2
- [28] N. Funabashi, H. Takaoka, K. Ozawa, T. Kamata, M. Uehara, I. Komuro, and Y. Kobayashi. Quantitative differentiation of lv myocardium with and without layer-specific fibrosis using mri in hypertrophic cardiomyopathy and layer-specific strain tte analysis. *Int Heart J*, 59(3):523–530, 2018. 3.3.2
- [29] H. Haraldsson, L. Wigstrom, M. Lundberg, A. F. Bolger, J. Engvall, T. Ebbers, and J. P. Kvitting. Improved estimation and visualization of two-dimensional myocardial strain rate using mr velocity mapping. *J Magn Reson Imaging*, 28(3):604–11, 2008. 3.3.3, 5.1.1
- [30] N. J. Pelc, M. Drangova, L. R. Pelc, Y. Zhu, D. C. Noll, B. S. Bowman, and R. J. Herfkens. Tracking of cyclic motion with phase-contrast cine mr velocity data. *J Magn Reson Imaging*, 5(3):339–45, 1995. 3.3.6
- [31] T. Røe Å, M. Ruud, E. K. Espe, O. Manfra, S. Longobardi, J. M. Aronsen, E. S. Nordén, T. Husebye, T. R. S. Kolstad, A. Cataliotti, G. Christensen, O. M. Sejersted, S. A. Niederer, GØ Andersen, I. Sjaastad, and W. E. Louch. Regional diastolic dysfunction in post-infarction heart failure: role of local mechanical load and serca expression. *Cardiovasc Res*, 115(4):752–764, 2019. 3.3.7, 3.4, 5.1.2, 5.1.3
- [32] A. H. Soepriatna, A. K. Yeh, A. D. Clifford, S. E. Bezci, G. D. O’Connell, and C. J. Goergen. Three-dimensional myocardial strain correlates with murine left ventricular remodelling severity post-infarction. *J R Soc Interface*, 16(160):20190570, 2019. 3.4
- [33] J. Kersten, A. M. Guleroglu, A. Rosenbohm, D. Buckert, A. C. Ludolph, C. Hackenbroch, M. Beer, and P. Bernhardt. Myocardial involvement and deformation abnormalities in idiopathic inflammatory myopathy assessed by cmr feature tracking. *Int J Cardiovasc Imaging*, 37(2):597–603, 2021. 3.4

- [34] Ahmed M. El Missiri. Echocardiographic assessment of left ventricular mechanical dyssynchrony a practical approach. *Echocardiography*, 2014. 3.4
- [35] J. He, W. Yang, W. Wu, S. Li, G. Yin, B. Zhuang, J. Xu, X. Sun, D. Zhou, B. Wei, A. Sirajuddin, Z. Teng, S. Zhao, F. Kureshi, and M. Lu. Early diastolic longitudinal strain rate at mri and outcomes in heart failure with preserved ejection fraction. *Radiology*, 301(3):582–592, 2021. 3.4.1
- [36] Yale University Courses. Confidence intervals. n.d. <http://www.stat.yale.edu/Courses/1997-98/101/confint.htm>, accessed 15.03.2024. 3.4.2
- [37] A. Banerjee, U. B. Chitnis, S. L. Jadhav, J. S. Bhawalkar, and S. Chaudhury. Hypothesis testing, type i and type ii errors. *Ind Psychiatry J*, 18(2):127–31, 2009. 3.4.3
- [38] A. Soghomonian, A. Dutour, N. Kachenoura, F. Thuny, A. Lasbleiz, P. Ancel, R. Cristofari, E. Jouve, U. Simeoni, F. Kober, M. Bernard, and B. Gaborit. Is increased myocardial triglyceride content associated with early changes in left ventricular function? a (1)h-mrs and mri strain study. *Front Endocrinol (Lausanne)*, 14:1181452, 2023. 5.1.2
- [39] R. Dragoi Galrinho, A. O. Ciobanu, R. C. Rimbas, C. G. Manole, B. M. Leena, and D. Vinereanu. New echocardiographic protocol for the assessment of experimental myocardial infarction in rats. *Maedica (Bucur)*, 10(2):85–90, 2015. 5.1.2
- [40] A. Petersen, S. N. Nagel, B. Hamm, T. Elgeti, and L. A. Schaafs. Cardiac magnetic resonance imaging in patients with left bundle branch block: Patterns of dyssynchrony and implications for late gadolinium enhancement imaging. *Front Cardiovasc Med*, 9:977414, 2022. 5.1.3

Appendix